

High- p_T Charged Hadron Suppression in $Au + Au$ Collisions at $\sqrt{s_{NN}} = 200$ GeV

S.S. Adler,⁵ S. Afanasiev,¹⁷ C. Aidala,⁵ N.N. Ajitanand,⁴³ Y. Akiba,^{20,38} J. Alexander,⁴³ R. Amirikas,¹² L. Aphecetche,⁴⁵ S.H. Aronson,⁵ R. Averbeck,⁴⁴ T.C. Awes,³⁵ R. Azmoun,⁴⁴ V. Babintsev,¹⁵ A. Baldissari,¹⁰ K.N. Barish,⁶ P.D. Barnes,²⁷ B. Bassalleck,³³ S. Bathe,³⁰ S. Batsouli,⁹ V. Baublis,³⁷ A. Bazilevsky,^{39,15} S. Belikov,^{16,15} Y. Berdnikov,⁴⁰ S. Bhagavatula,¹⁶ J.G. Boissevain,²⁷ H. Borel,¹⁰ S. Borenstein,²⁵ M.L. Brooks,²⁷ D.S. Brown,³⁴ N. Bruner,³³ D. Bucher,³⁰ H. Buesching,³⁰ V. Bumazhnov,¹⁵ G. Bunce,^{5,39} J.M. Burward-Hoy,^{26,44} S. Butsyk,⁴⁴ X. Camard,⁴⁵ J.-S. Chai,¹⁸ P. Chand,⁴ W.C. Chang,² S. Chernichenko,¹⁵ C.Y. Chi,⁹ J. Chiba,²⁰ M. Chiu,⁹ I.J. Choi,⁵² J. Choi,¹⁹ R.K. Choudhury,⁴ T. Chujo,⁵ V. Cianciolo,³⁵ Y. Cobigo,¹⁰ B.A. Cole,⁹ P. Constantin,¹⁶ D.G. d'Enterria,⁴⁵ G. David,⁵ H. Delagrange,⁴⁵ A. Denisov,¹⁵ A. Deshpande,³⁹ E.J. Desmond,⁵ O. Dietzsch,⁴¹ O. Drapier,²⁵ A. Drees,⁴⁴ R. du Rietz,²⁹ A. Durum,¹⁵ D. Dutta,⁴ Y.V. Efremenko,³⁵ K. El Chenawi,⁴⁹ A. Enokizono,¹⁴ H. En'yo,^{38,39} S. Esumi,⁴⁸ L. Ewell,⁵ D.E. Fields,^{33,39} F. Fleuret,²⁵ S.L. Fokin,²³ B.D. Fox,³⁹ Z. Fraenkel,⁵¹ J.E. Frantz,⁹ A. Franz,⁵ A.D. Frawley,¹² S.-Y. Fung,⁶ S. Garpman,^{29,*} T.K. Ghosh,⁴⁹ A. Glenn,⁴⁶ G. Gogoberidze,⁴⁶ M. Gonin,²⁵ J. Gosset,¹⁰ Y. Goto,³⁹ R. Granier de Cassagnac,²⁵ N. Grau,¹⁶ S.V. Greene,⁴⁹ M. Grosse Perdekamp,³⁹ W. Guryan,⁵ H.-Å. Gustafsson,²⁹ T. Hachiya,¹⁴ J.S. Haggerty,⁵ H. Hamagaki,⁸ A.G. Hansen,²⁷ E.P. Hartouni,²⁶ M. Harvey,⁵ R. Hayano,⁸ X. He,¹³ M. Heffner,²⁶ T.K. Hemmick,⁴⁴ J.M. Heuser,⁴⁴ M. Hibino,⁵⁰ J.C. Hill,¹⁶ W. Holzmann,⁴³ K. Homma,¹⁴ B. Hong,²² A. Hoover,³⁴ T. Ichihara,^{38,39} V.V. Ikonnikov,²³ K. Imai,^{24,38} D. Isenhower,¹ M. Ishihara,³⁸ M. Issah,⁴³ A. Isupov,¹⁷ B.V. Jacak,⁴⁴ W.Y. Jang,²² Y. Jeong,¹⁹ J. Jia,⁴⁴ O. Jinnouchi,³⁸ B.M. Johnson,⁵ S.C. Johnson,²⁶ K.S. Joo,³¹ D. Jouan,³⁶ S. Kametani,^{8,50} N. Kamihara,^{47,38} J.H. Kang,⁵² S.S. Kapoor,⁴ K. Katou,⁵⁰ S. Kelly,⁹ B. Khachaturov,⁵¹ A. Khanzadeev,³⁷ J. Kikuchi,⁵⁰ D.H. Kim,³¹ D.J. Kim,⁵² D.W. Kim,¹⁹ E. Kim,⁴² G.-B. Kim,²⁵ H.J. Kim,⁵² E. Kistenev,⁵ A. Kiyomichi,⁴⁸ K. Kiyoyama,³² C. Klein-Boesing,³⁰ H. Kobayashi,^{38,39} L. Kochenda,³⁷ V. Kochetkov,¹⁵ D. Koehler,³³ T. Kohama,¹⁴ M. Kopytine,⁴⁴ D. Kotchetkov,⁶ A. Kozlov,⁵¹ P.J. Kroon,⁵ C.H. Kuberg,^{1,27} K. Kurita,³⁹ Y. Kuroki,⁴⁸ M.J. Kweon,²² Y. Kwon,⁵² G.S. Kyle,³⁴ R. Lacey,⁴³ V. Ladygin,¹⁷ J.G. Lajoie,¹⁶ A. Lebedev,^{16,23} S. Leckey,⁴⁴ D.M. Lee,²⁷ S. Lee,¹⁹ M.J. Leitch,²⁷ X.H. Li,⁶ H. Lim,⁴² A. Litvinenko,¹⁷ M.X. Liu,²⁷ Y. Liu,³⁶ C.F. Maguire,⁴⁹ Y.I. Makdisi,⁵ A. Malakhov,¹⁷ V.I. Manko,²³ Y. Mao,^{7,38} G. Martinez,⁴⁵ M.D. Marx,⁴⁴ H. Masui,⁴⁸ F. Matathias,⁴⁴ T. Matsumoto,^{8,50} P.L. McGaughey,²⁷ E. Melnikov,¹⁵ F. Messer,⁴⁴ Y. Miake,⁴⁸ J. Milan,⁴³ T.E. Miller,⁴⁹ A. Milov,^{44,51} S. Mioduszewski,⁵ R.E. Mischke,²⁷ G.C. Mishra,¹³ J.T. Mitchell,⁵ A.K. Mohanty,⁴ D.P. Morrison,⁵ J.M. Moss,²⁷ F. Mühlbacher,⁴⁴ D. Mukhopadhyay,⁵¹ M. Muniruzzaman,⁶ J. Murata,^{38,39} S. Nagamiya,²⁰ J.L. Nagle,⁹ T. Nakamura,¹⁴ B.K. Nandi,⁶ M. Nara,⁴⁸ J. Newby,⁴⁶ P. Nilsson,²⁹ A.S. Nyatin,²³ J. Nystrand,²⁹ E. O'Brien,⁵ C.A. Ogilvie,¹⁶ H. Ohnishi,^{5,38} I.D. Ojha,^{49,3} K. Okada,³⁸ M. Ono,⁴⁸ V. Onuchin,¹⁵ A. Oskarsson,²⁹ I. Otterlund,²⁹ K. Oyama,⁸ K. Ozawa,⁸ D. Pal,⁵¹ A.P.T. Palounek,²⁷ V.S. Pantuev,⁴⁴ V. Papavassiliou,³⁴ J. Park,⁴² A. Parmar,³³ S.F. Pate,³⁴ T. Peitzmann,³⁰ J.-C. Peng,²⁷ V. Peresedov,¹⁷ C. Pinkenburg,⁵ R.P. Pisani,⁵ F. Plasil,³⁵ M.L. Purschke,⁵ A.K. Purwar,⁴⁴ J. Rak,¹⁶ I. Ravinovich,⁵¹ K.F. Read,^{35,46} M. Reuter,⁴⁴ K. Reygers,³⁰ V. Riabov,^{37,40} Y. Riabov,³⁷ G. Roche,²⁸ A. Romana,²⁵ M. Rosati,¹⁶ P. Rosnet,²⁸ S.S. Ryu,⁵² M.E. Sadler,¹ N. Saito,^{38,39} T. Sakaguchi,^{8,50} M. Sakai,³² S. Sakai,⁴⁸ V. Samsonov,³⁷ L. Sanfratello,³³ R. Santo,³⁰ H.D. Sato,^{24,38} S. Sato,^{5,48} S. Sawada,²⁰ Y. Schutz,⁴⁵ V. Semenov,¹⁵ R. Seto,⁶ M.R. Shaw,^{1,27} T.K. Shea,⁵ T.-A. Shibata,^{47,38} K. Shigaki,^{14,20} T. Shiina,²⁷ C.L. Silva,⁴¹ D. Silvermyr,^{27,29} K.S. Sim,²² C.P. Singh,³ V. Singh,³ M. Sivertz,⁵ A. Soldatov,¹⁵ R.A. Soltz,²⁶ W.E. Sondheim,²⁷ S.P. Sorensen,⁴⁶ I.V. Sourikova,⁵ F. Staley,¹⁰ P.W. Stankus,³⁵ E. Stenlund,²⁹ M. Stepanov,³⁴ A. Ster,²¹ S.P. Stoll,⁵ T. Sugitate,¹⁴ J.P. Sullivan,²⁷ E.M. Takagui,⁴¹ A. Taketani,^{38,39} M. Tamai,⁵⁰ K.H. Tanaka,²⁰ Y. Tanaka,³² K. Tanida,³⁸ M.J. Tannenbaum,⁵ P. Tarján,¹¹ J.D. Tepe,^{1,27} T.L. Thomas,³³ J. Tojo,^{24,38} H. Torii,^{24,38} R.S. Towell,¹ I. Tserruya,⁵¹ H. Tsuruoka,⁴⁸ S.K. Tuli,³ H. Tydesjö,²⁹ N. Tyurin,¹⁵ H.W. van Hecke,²⁷ J. Velkovska,^{5,44} M. Velkovsky,⁴⁴ L. Villatte,⁴⁶ A.A. Vinogradov,²³ M.A. Volkov,²³ E. Vznuzdaev,³⁷ X.R. Wang,¹³ Y. Watanabe,^{38,39} S.N. White,⁵ F.K. Wohn,¹⁶ C.L. Woody,⁵ W. Xie,⁶ Y. Yang,⁷ A. Yanovich,¹⁵ S. Yokkaichi,^{38,39} G.R. Young,³⁵ I.E. Yushmanov,²³ W.A. Zajc,^{9,†} C. Zhang,⁹ S. Zhou,^{7,51} and L. Zolin¹⁷

(PHENIX Collaboration)

¹Abilene Christian University, Abilene, TX 79699, USA

²Institute of Physics, Academia Sinica, Taipei 11529, Taiwan

³Department of Physics, Banaras Hindu University, Varanasi 221005, India

⁴Bhabha Atomic Research Centre, Bombay 400 085, India

⁵Brookhaven National Laboratory, Upton, NY 11973-5000, USA

⁶University of California - Riverside, Riverside, CA 92521, USA

⁷China Institute of Atomic Energy (CIAE), Beijing, People's Republic of China

⁸Center for Nuclear Study, Graduate School of Science, University of Tokyo, 7-3-1 Hongo, Bunkyo, Tokyo 113-0033, Japan
⁹Columbia University, New York, NY 10027 and Nevis Laboratories, Irvington, NY 10533, USA
¹⁰Dapnia, CEA Saclay, F-91191, Gif-sur-Yvette, France
¹¹Debrecen University, H-4010 Debrecen, Egyetem tér 1, Hungary
¹²Florida State University, Tallahassee, FL 32306, USA
¹³Georgia State University, Atlanta, GA 30303, USA
¹⁴Hiroshima University, Kagamiyama, Higashi-Hiroshima 739-8526, Japan
¹⁵Institute for High Energy Physics (IHEP), Protvino, Russia
¹⁶Iowa State University, Ames, IA 50011, USA
¹⁷Joint Institute for Nuclear Research, 141980 Dubna, Moscow Region, Russia
¹⁸KAERI, Cyclotron Application Laboratory, Seoul, South Korea
¹⁹Kangnung National University, Kangnung 210-702, South Korea
²⁰KEK, High Energy Accelerator Research Organization, Tsukuba-shi, Ibaraki-ken 305-0801, Japan
²¹KFKI Research Institute for Particle and Nuclear Physics (RMKI), H-1525 Budapest 114, POBox 49, Hungary
²²Korea University, Seoul, 136-701, Korea
²³Russian Research Center "Kurchatov Institute", Moscow, Russia
²⁴Kyoto University, Kyoto 606, Japan
²⁵Laboratoire Leprince-Ringuet, Ecole Polytechnique, CNRS-IN2P3, Route de Saclay, F-91128, Palaiseau, France
²⁶Lawrence Livermore National Laboratory, Livermore, CA 94550, USA
²⁷Los Alamos National Laboratory, Los Alamos, NM 87545, USA
²⁸LPC, Université Blaise Pascal, CNRS-IN2P3, Clermont-Fd, 63177 Aubiere Cedex, France
²⁹Department of Physics, Lund University, Box 118, SE-221 00 Lund, Sweden
³⁰Institut fuer Kernphysik, University of Muenster, D-48149 Muenster, Germany
³¹Myongji University, Yongin, Kyonggido 449-728, Korea
³²Nagasaki Institute of Applied Science, Nagasaki-shi, Nagasaki 851-0193, Japan
³³University of New Mexico, Albuquerque, NM, USA
³⁴New Mexico State University, Las Cruces, NM 88003, USA
³⁵Oak Ridge National Laboratory, Oak Ridge, TN 37831, USA
³⁶IPN-Orsay, Universite Paris Sud, CNRS-IN2P3, BP1, F-91406, Orsay, France
³⁷PNPI, Petersburg Nuclear Physics Institute, Gatchina, Russia
³⁸RIKEN (The Institute of Physical and Chemical Research), Wako, Saitama 351-0198, JAPAN
³⁹RIKEN BNL Research Center, Brookhaven National Laboratory, Upton, NY 11973-5000, USA
⁴⁰St. Petersburg State Technical University, St. Petersburg, Russia
⁴¹Universidade de São Paulo, Instituto de Física, Caixa Postal 66318, São Paulo CEP05315-970, Brazil
⁴²System Electronics Laboratory, Seoul National University, Seoul, South Korea
⁴³Chemistry Department, Stony Brook University, SUNY, Stony Brook, NY 11794-3400, USA
⁴⁴Department of Physics and Astronomy, Stony Brook University, SUNY, Stony Brook, NY 11794, USA
⁴⁵SUBATECH (Ecole des Mines de Nantes, CNRS-IN2P3, Université de Nantes) BP 20722 - 44307, Nantes, France
⁴⁶University of Tennessee, Knoxville, TN 37996, USA
⁴⁷Department of Physics, Tokyo Institute of Technology, Tokyo, 152-8551, Japan
⁴⁸Institute of Physics, University of Tsukuba, Tsukuba, Ibaraki 305, Japan
⁴⁹Vanderbilt University, Nashville, TN 37235, USA
⁵⁰Waseda University, Advanced Research Institute for Science and Engineering, 17 Kikui-cho, Shinjuku-ku, Tokyo 162-0044, Japan
⁵¹Weizmann Institute, Rehovot 76100, Israel
⁵²Yonsei University, IPAP, Seoul 120-749, Korea

(Dated: January 24, 2019)

The PHENIX experiment at RHIC has measured charged hadron yields at mid-rapidity over a wide range of transverse momentum ($0.5 < p_T < 10$ GeV/c) in $Au + Au$ collisions at $\sqrt{s_{NN}} = 200$ GeV. The data are compared to π^0 measurements from the same experiment. For both charged hadrons and neutral pions, the yields per nucleon-nucleon collision are significantly suppressed in central compared to peripheral and nucleon-nucleon collisions. The suppression sets in gradually and increases with increasing centrality of the collisions. Above 4-5 GeV/c in p_T , a constant and almost identical suppression of charged hadrons and π^0 's is observed. The p_T spectra are compared to published spectra from $Au + Au$ at $\sqrt{s_{NN}} = 130$ in terms of x_T scaling. Central and peripheral π^0 as well as peripheral charged spectra exhibit the same x_T scaling as observed in $p + p$ data.

PACS numbers: 25.75.Dw

*Deceased

†PHENIX Spokesperson:zajc@nevis.columbia.edu

I. INTRODUCTION

Lattice Quantum-Chromo-Dynamic (QCD) calculations predict a new state of matter of deconfined quarks and gluons at an energy density exceeding $\sim 1 \text{ GeV}/\text{fm}^3$ [1]. It has long been suggested that such a “quark gluon plasma” may be produced in collisions between ultra-relativistic heavy nuclei [2]. Indeed, measurements of transverse energy produced in high energy $Pb + Pb$ and $Au + Au$ collision suggest that energy densities above $3 \text{ GeV}/\text{fm}^3$ at SPS [3] and $5 \text{ GeV}/\text{fm}^3$ at RHIC [4, 5] have been reached. However, this conclusion relies on model assumptions [6, 7, 8, 9] to relate the properties of the hadronic final state to the initial state dynamics.

The spectra of high transverse momentum (p_T) hadrons resulting from the fragmentation of hard-scattered partons potentially provide a direct probe of the properties of the initial state. Theoretical calculations show that the outgoing high- p_T partons radiate substantially more energy when propagating through dense matter than when propagating in the vacuum, resulting in a softening of the hadron p_T spectrum [10], with the energy loss of the partons depending on the gluon density of the matter [11, 12]. Formation time considerations suggest that hard scattered partons are “produced” at the earliest stage of the collision, thus directly probe the dense matter from the time of their creation. Therefore, high- p_T hadron production can be used as a tool to understand the properties of the dense matter [12, 13, 14].

At the energies reached at the Relativistic Heavy Ion Collider (RHIC), high- p_T hadrons are copiously produced. In nucleon-nucleon collisions, it has been well established that hadrons with $p_T \geq 2 \text{ GeV}/c$ result primarily from the fragmentation of hard-scattered partons, and that the p_T spectra of these hadrons can be calculated using perturbative QCD (pQCD) [15, 16]. Initial measurements of hadron p_T spectra in $Au + Au$ collisions at $\sqrt{s_{NN}} = 130 \text{ GeV}$ led to the discovery of a substantial suppression of hadron yields per nucleon-nucleon collision relative to pp data [17, 18, 19]. Data from $\sqrt{s_{NN}} = 200 \text{ GeV}$ confirm these results [20, 21, 22]. The suppression is observed in central but not in peripheral collisions. These observations are consistent with pQCD-inspired modelling of parton energy loss in dense matter [23, 24]. However, alternative interpretations that do not assume the formation of a deconfined phase have been proposed based on the modifications of the parton distribution functions in the initial state [25] or final-state hadronic interactions [26].

In addition to hadron suppression, an unexpectedly large fraction of baryons has been observed in central $Au + Au$ collisions for p_T up to $4\text{--}5 \text{ GeV}/c$ [27, 28, 29], which complicates the interpretation of the high p_T results. The observed baryon to meson ratio from PHENIX [28] is inconsistent with jet fragmentation in

$p + p$ [30] and e^+e^- collisions [31]. While the origin of this effect is unclear, it could point towards bulk particle production (“soft physics”) contributing to the p_T spectra out to $4\text{--}5 \text{ GeV}/c$. It has been suggested that coalescence of thermalized quarks combining with energy loss of hard-scattered partons can account for the unusual particle composition, which shifts the region dominated by hard-scattering to higher p_T [32].

Systematic measurements of the p_T , centrality, particle species, and $\sqrt{s_{NN}}$ dependence of the suppression can constrain competing descriptions of high- p_T hadron production. In this paper, we present new data on inclusive charged hadron production for $0.5 < p_T < 10 \text{ GeV}/c$, measured over a broad range of centrality in $Au + Au$ collisions at $\sqrt{s_{NN}} = 200 \text{ GeV}$ by the PHENIX Collaboration at RHIC. These data are compared to data on neutral pion production [21] and to data from $Au + Au$ collisions at $\sqrt{s_{NN}} = 130 \text{ GeV}$ [17, 19], all measured within the same experiment.

The remainder of the paper is organized as follows. Section II gives a detailed account of the charged particle analysis. Centrality and p_T dependence of the charged hadron p_T spectra are discussed in Section III A. Section III B studies the charged hadron suppression and compares the results to π^0 data. In Section III C, we discuss the $\sqrt{s_{NN}}$ dependence of both charged hadron and neutral pion production and test possible x_T -scaling. A summary is given in Section IV.

II. DATA ANALYSIS

In this section, we describe the PHENIX experiment, event selection and the charged particle analysis. We focus on the reconstruction of p_T spectra above $4.5 \text{ GeV}/c$.

A. PHENIX Detector

The PHENIX experiment consists of four spectrometer arms – two around mid-rapidity (the central arms) and two at forward rapidity (the muon arms) – and a set of global detectors. The central arm and south Muon arm detectors were completed in 2001 and took data during $Au + Au$ operation of RHIC the same year (RUN-2). The layout of the PHENIX experiment during RUN-2 is shown in Fig. 1. Each central arm covers the pseudo-rapidity range $|\eta| < 0.35$ and 90 degrees in azimuthal angle ϕ . In each of the central arms, charged particles are tracked by a drift chamber (DC) positioned from 2.0 to 2.4m radially outward from the beam axis and 2 or 3 layers of pixel pad chambers (PC1, (PC2), PC3 located at 2.4m, (4.2m), 5m in radial direction, respectively). Particle identification is provided by ring imaging Cerenkov counters (RICH), a time of flight scintillator wall (TOF), and two types of electromagnetic calorimeters (lead scintillator (PBSC) and lead glass (PBGL)). The magnetic field for the central spectrometer is axially

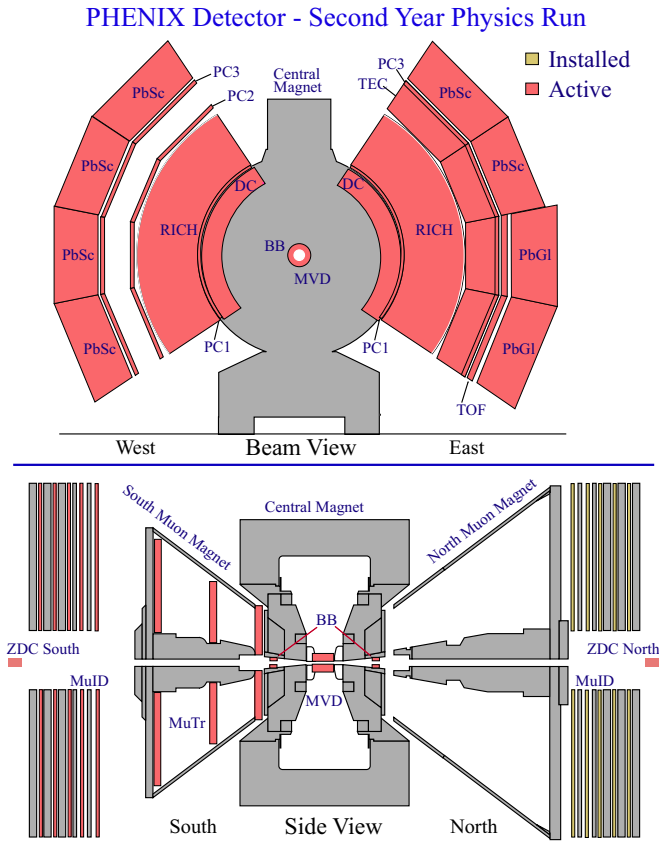


FIG. 1: PHENIX experimental layout for the $Au + Au$ run in 2001. The top panel shows the PHENIX central arm spectrometers viewed along the beam axis. The bottom panel shows a side view of the PHENIX muon arm spectrometers.

symmetric around the beam axis. Its component parallel to the beam axis has an approximately Gaussian dependence on the radial distance from the beam axis, dropping from 0.48 T at the center to 0.096 T (0.048 T) at the inner (outer) radius of the DC. A pair of Zero-Degree Calorimeters (ZDC) and a pair of Beam-Beam Counters (BBC) were used for global event characterization. Further details about the design and performance of PHENIX can be found in [33].

B. Event Selection

During RUN-2, PHENIX sampled an integrated luminosity of $24 \mu b^{-1}$ for $Au + Au$ collisions at $\sqrt{s_{NN}} = 200$ GeV. Minimum bias events were selected by a coincidence between the ZDCs and the BBCs. This selection corresponds to $92.2^{+2.5\%}_{-3.0\%}$ of the 6.9 barn $Au + Au$ inelastic cross section. The event centrality is determined by correlating the charge detected in the BBCs with the energy measured in the ZDCs. Two sets of centrality definitions are used in this analysis: a “Fine” set of centralities, which corresponds to 0-5%, ..., 15-20%, 20-30%, ..., 80-92%, and a “Coarse” set of centralities, which corre-

TABLE I: Centrality classes, average nuclear overlap function, average number of $N + N$ collisions, and average number of participant nucleons obtained from a Glauber Monte-Carlo simulation of the BBC and ZDC responses for $Au + Au$ at $\sqrt{s_{NN}} = 200$ GeV. Each centrality class is expressed as a percentage of $\sigma_{AuAu} = 6.9$ b. Two sets of centrality definitions are used in this analysis: a “Fine” set of centralities, which corresponds to 0-5%, ..., 15-20%, 20-30%, ..., 80-92%, and a “Coarse” set of centralities, which corresponds to 0-10%, 10-20%, 20-30%, ..., 80-92%.

Centrality	$\langle N_{coll} \rangle$	$\langle N_{part} \rangle$	$\langle T_{AuAu} \rangle (mb^{-1})$
0 - 5%	1065 ± 105.5	351.4 ± 2.9	25.37 ± 1.77
5 - 10%	854.4 ± 82.1	299 ± 3.8	20.13 ± 1.36
10 - 15%	672.4 ± 66.8	253.9 ± 4.3	16.01 ± 1.15
15 - 20%	532.7 ± 52.1	215.3 ± 5.3	12.68 ± 0.86
0 - 10%	955.4 ± 93.6	325.2 ± 3.3	22.75 ± 1.56
10 - 20%	602.6 ± 59.3	234.6 ± 4.7	14.35 ± 1.00
20 - 30%	373.8 ± 39.6	166.6 ± 5.4	8.90 ± 0.72
30 - 40%	219.8 ± 22.6	114.2 ± 4.4	5.23 ± 0.44
40 - 50%	120.3 ± 13.7	74.4 ± 3.8	2.86 ± 0.28
50 - 60%	61.0 ± 9.9	45.5 ± 3.3	1.45 ± 0.23
60 - 70%	28.5 ± 7.6	25.7 ± 3.8	0.68 ± 0.18
70 - 80%	12.4 ± 4.2	13.4 ± 3.0	0.30 ± 0.10
80 - 92%	4.9 ± 1.2	6.3 ± 1.2	0.12 ± 0.03
60 - 92%	14.5 ± 4	14.5 ± 2.5	0.35 ± 0.10
min. bias	257.8 ± 25.4	109.1 ± 4.1	6.14 ± 0.45

sponds to 0-10%, 10-20%, 20-30%, ..., 80-92%. A Glauber model Monte-Carlo simulation [34, 35] that includes the responses of BBC and ZDC gives an estimate of the average number of binary collisions $\langle N_{coll} \rangle$, participating nucleons $\langle N_{part} \rangle$ and nuclear overlap function $\langle T_{AuAu} \rangle$ for each centrality class. The calculated values of $\langle N_{coll} \rangle$, $\langle N_{part} \rangle$ and $\langle T_{AuAu} \rangle$ for each centrality class are listed in Table I.

In addition to the event selection, the BBCs also allow us to reconstruct the collision vertex in the beam direction (z) with a resolution of 0.5 cm. An offline z -vertex cut, $|z_{vtx}| < 30$ cm, was applied to the minimum bias events. After this selection, a total of 27×10^6 minimum bias $Au + Au$ events were analyzed to obtain the charged hadron spectra presented in this paper.

C. Charged Particle Tracking and Momentum Measurement

Charged hadron tracks are measured using information from the DC, PC1, PC2 and PC3 detectors of the west central-arm and the BBC. The projections of the charged particle trajectories into a plane perpendicular to the beam axis are detected typically in 12 wire planes in the DC. The wire planes spaced at 0.6 cm intervals along the radial direction from the beam axis. Each wire provides a projective measurement, with better than $150 \mu m$ spacial resolution in the azimuthal (ϕ) direction. Eight additional wire planes in the DC provide stereoscopic projections, which together with the space point

measured at the PC1 and the vertex position measured by the BBC determine the polar angle of the track. Trajectories are confirmed by requiring matching hits at both PC2 and PC3 to reduce the secondary background.

Tracks are then projected back to the collision vertex through the magnetic field to determine the momentum \vec{p} . The transverse momentum p_T is related to the deflection angle α measured at the DC with respect to an infinite momentum trajectory. For tracks emitted perpendicular to the beam axis, this relation can be approximated by

$$\alpha \simeq \frac{K}{p_T} \quad , \quad (1)$$

where $K = 87$ mrad GeV/c is the effective field integral.

The momentum scale is verified by comparing the known proton mass to the value measured for charged particles identified as protons from their time-of-flight. The flight-time is measured in the TOF detector, which cover $\pi/4$ of the azimuthal acceptance in the east arm. The absolute value of the momentum scale is known to be better than 0.7%.

The momentum resolution is directly related to the α resolution,

$$\begin{aligned} \delta p/p &= \delta\alpha/\alpha & (2) \\ &= \frac{1}{K} \sqrt{\left(\frac{\sigma_{ms}}{\beta}\right)^2 + (\sigma_\alpha p)^2} \quad , \end{aligned}$$

where $\delta\alpha$ is the measured angular spread, which can be decomposed into the contribution from multiple scattering (σ_{ms}) and the contribution from the intrinsic pointing resolution (σ_α) of the DC. At high p_T , σ_α is the dominating contribution, i.e. $\delta\alpha/\alpha \simeq \sigma_\alpha$. We measure $\sigma_\alpha \approx 0.84 \pm 0.05$ mrad/(GeV/c) using zero field data, where we select high-momentum tracks by requiring energetic hadronic showers in the electromagnetic calorimeters. The width of the proton mass as function of p_T independently confirms the momentum resolution. In summary, the momentum resolution is determined to be $\delta p/p \simeq 0.7\% \oplus 1.0\% p$ (GeV/c). Further details on track reconstruction and momentum determination can be found in [36].

D. Background Rejection and Subtraction

Approximately 95% of the tracks reconstructed by the DC originate from the event vertex. The remainder have to be investigated as potential background to the charged particle measurement. The main background sources include secondary particles from decays and e^+e^- pairs from the conversion of photons in materials between the vertex and the DC. Depending on how close the conversion or decay point is to the DC, or depending on the Q-value of the decay, these tracks may have a small deflection angle α at the DC. Thus, according to Eq. 1, they

are incorrectly assigned a large momentum. In this analysis, the p_T range over which charged particle production is accessible in PHENIX is limited by this background. We exploit the track match to PC2 and PC3 to reject as much of the background as possible, then employ a statistical method to measure and subtract the irreducible background.

For primary tracks, the distance in both the $r\phi$ and the z direction between the track projection point and the measured PC hit position is approximately Gaussian with a mean of 0 and a width given by,

$$\sigma_{match} = \sqrt{\sigma_{det}^{match^2} + \left(\frac{\sigma_{ms}^{match}}{p\beta}\right)^2} \quad , \quad (3)$$

where σ_{det}^{match} is the finite detector resolution (which includes DC pointing (or α) resolution and the PC2, PC3 spacial resolution), and σ_{ms}^{match} is the multiple scattering contribution.

Despite being incorrectly reconstructed with large p_T , the majority of the background particles have low momenta. While travelling from the DC to the PC2 and PC3, they multiple scatter and receive an additional deflection from the fringe field. This causes a correlated deflection between the measured positions at PC2, PC3, and the projections calculated from tracks measured by the DC and PC1. The displacements in $r\phi$ and z directions are represented by D_ϕ and D_z . Since the residual bend depends on the z component of the fringe field, which decreases rapidly at large $|\eta|$, a fiducial cut of $|\eta| < 0.18$ was applied to ensure that the residual bend due to the fringe field is almost independent of z . We focus on the displacement in $r\phi$, D_ϕ , which are large for low momentum tracks due to the residual bend. The D_ϕ 's at PC2 and PC3 are correlated with each other, as shown in Fig. 2. Most of the tracks lie in a narrow window around the diagonal line. The width of this window is given by the PC2 and PC3 detector resolutions, which are of the order of a few millimeters. Multiple scattering and residual bend broaden the matching distribution along the diagonal line. To optimize background rejection, we define two orthogonal projections,

$$\begin{aligned} D_\phi^+ &= \frac{1}{\sqrt{2}}(D_\phi^{pc2} + D_\phi^{pc3}) & (4) \\ D_\phi^- &= \frac{1}{\sqrt{2}}(D_\phi^{pc2} - D_\phi^{pc3}) \end{aligned}$$

D_ϕ^+ is the variable along the correlated direction, D_ϕ^- is the direction normal to D_ϕ^+ . A $\pm 2\sigma$ cut on these variables is applied in the data analysis. In the remaining discussion, unless stated otherwise, only tracks satisfying these cuts are included.

After matching cuts, the background level is less than 6% for $p_T < 4$ GeV/c, but increases rapidly at higher p_T . For $4 < p_T < 10$ GeV/c, the most significant remaining background sources are e^+e^- from conversion of photons close to the DC and particles from weak decays of

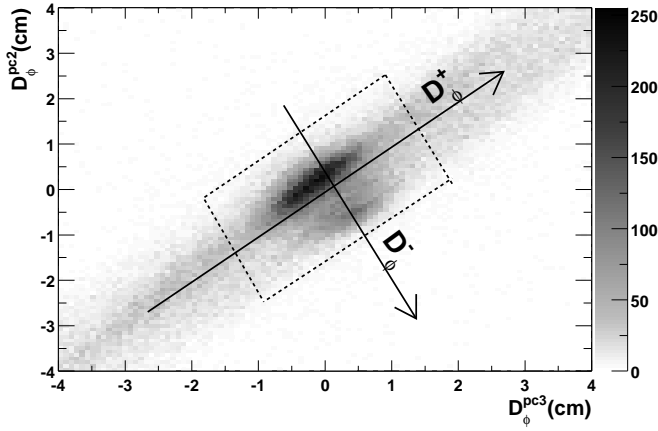


FIG. 2: D_{ϕ}^{pc2} (the difference between projection and hit location in $r\phi$ direction at PC2) versus D_{ϕ}^{pc3} in centimeters for tracks with reconstructed $p_T > 4 \text{ GeV}/c$. PC2, PC3 matching differences are correlated, with signal tracks peaked around 0 and background tracks extend along the D_{ϕ}^+ direction. The double-peak structure along D_{ϕ}^- is related to the finite granularity of PC2 and PC3 pads. The positive directions of D_{ϕ}^+ and D_{ϕ}^- are indicated by the arrow. A $\pm 2\sigma$ cut on these variables is illustrated by the box region inside the dashed lines.

long lived particles, mainly of K^\pm and K_L^0 . These backgrounds are estimated and subtracted separately from the D_{ϕ}^+ distribution for all tracks, as will be discussed in the rest of this section.

To separate the two background sources, we take advantage of the RICH to tag electrons. Charged particles with velocities above the Cherenkov threshold $\gamma_{th} = 35$ (CO_2 radiator) will emit Cherenkov photons, which are detected by photon multiplier tubes (PMT) in the RICH [37]. We characterize the Cherenkov photon yield for a charged particle by N_{PMT} , the number of PMTs with signals above threshold associated to the track. For reconstructed electrons ($p_T > 150 \text{ MeV}/c$), the average number of associated PMTs is $\langle N_{PMT} \rangle \approx 4.5$. The probability to find at least one PMT above threshold is more than 99%. For pions, the Cherenkov threshold is $4.8 \text{ GeV}/c$, and the number of associated PMTs reaches its asymptotic value only well above $10 \text{ GeV}/c$; $\langle N_{PMT} \rangle$ increases from 1.4 at $6 \text{ GeV}/c$ to 2.8 at $8 \text{ GeV}/c$ and 3.6 at $10 \text{ GeV}/c$.

Tracks (N_R) with at least one associated RICH PMT contain both conversion electrons and real pions. Their matching distributions in D_{ϕ}^+ are presented in Fig. 3 for a sample range of $6 < p_T < 7 \text{ GeV}/c$. Also shown is the matching distribution for conversion electrons from Monte-Carlo simulation. The contributions from pions and electrons are clearly distinguishable. For pions with $p_T < 10 \text{ GeV}/c$, $\langle N_{PMT} \rangle$ has not reached its asymptotic value. A requirement of $N_{PMT} \geq 5$ rejects most of the pions while preserving a well-defined fraction (R_e) of the electrons. To measure R_e from the data, we select tracks

with an apparent $p_T > 10 \text{ GeV}/c$.¹ The fraction of tracks with $N_{PMT} \geq 5$ is measured to be $R_e = 0.458 \pm 0.05$. Both Monte-Carlo and data show a small variation of R_e with p_T and centrality. This variation is included in the error on R_e . The total electron background is calculated using tracks with $N_{PMT} \geq 5$ (N_e) as, N_e/R_e . The number of real pions in the RICH-associated sample for each p_T bin is then calculated as,

$$S_R = N_R - \frac{N_e}{R_e} \quad . \quad (5)$$

With this method, a small fraction of genuine pions, which satisfy $N_{PMT} \geq 5$, is subtracted. This fraction is negligible below $7 \text{ GeV}/c$, but increases rapidly towards higher p_T . This loss is corrected using the PHENIX Monte-Carlo simulation. In this case, a 100% error on the correction is assigned.

The sample of tracks (N_{NR}) with no associated RICH PMT contains a mixture of π, K, p , contaminated by the decay background. Their matching distributions in D_{ϕ}^+ are shown in Fig. 4 for $6 < p_T < 7 \text{ GeV}/c$, together with the matching distribution for decay particles from MC simulation. A Monte-Carlo study shows that the apparent momentum of these tracks is nearly uncorrelated with true momentum and therefore the distribution of this background in D_{ϕ}^+ is nearly independent of the apparent momentum. We select a nearly pure background sample using tracks with reconstructed $p_T > 10 \text{ GeV}/c$ and measure the ratio of the number of tracks passing a $|D_{\phi}^+| < 2\sigma$ cut to tracks in the interval $3\sigma < |D_{\phi}^+| < 9\sigma$:

$$R_{decay} = \frac{N_{NR}(p_T > 10 \text{ GeV}/c, |D_{\phi}^+| < 2\sigma)}{N_{NR}(p_T > 10 \text{ GeV}/c, 3\sigma < |D_{\phi}^+| < 9\sigma)} \quad (6)$$

$$= 0.424 \pm 0.05$$

The error quoted takes into account the small variation of R_{decay} with p_T and centrality. Since the average yield of real hadrons in this interval is small, we estimate the decay contribution as a function of p_T to be $N_{NR}(3\sigma < |D_{\phi}^+| < 9\sigma) \times R_{decay}$. Finally, the signal is calculated as,

$$S_{NR} = N_{NR}(|D_{\phi}^+| < 2\sigma) - \quad (7)$$

$$N_{NR}(3\sigma < |D_{\phi}^+| < 9\sigma) \times R_{decay}$$

Figure 5 gives the total signal, obtained as $S_R + S_{NR}$, with the decay and conversion background subtracted. On the right hand side, the signal-to-background ratio is shown. The background increases with increasing p_T . At

¹ In this p_T range, the background yield decrease slowly with p_T , while the true π yield decreases rapidly as p_T increases. By comparing the measured π^0 spectrum from PHENIX [21] with the charged hadron spectrum before background subtraction at $p_T > 10 \text{ GeV}/c$, the integrated signal yield is estimated to be less than 3% and thus may be neglected.

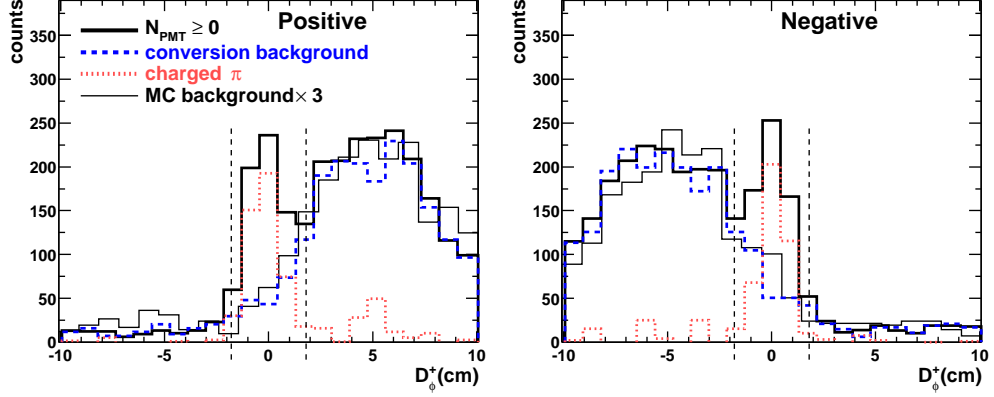


FIG. 3: An illustration of the track match in D_ϕ^+ for tracks with associated RICH PMTs and $6 < p_T < 7$ GeV/c. The matching distributions are shown for minimum bias events and separately for positive (left) and negative (right) charged tracks. The first three distributions represent the raw counts for all tracks with RICH association (thick solid line), estimated conversion backgrounds (dashed line) and charged pions (dot-dashed line) that were obtained by subtracting the dashed line from the solid line. The thin solid line represents the matching distribution of background electrons from Monte-carlo simulation, arbitrarily scaled to match the data. The 2σ matching window are illustrated by the vertical dashed line. Since e^+ and e^- are deflected in opposite directions by the fringe field, they are shifted to positive and negative directions, respectively.

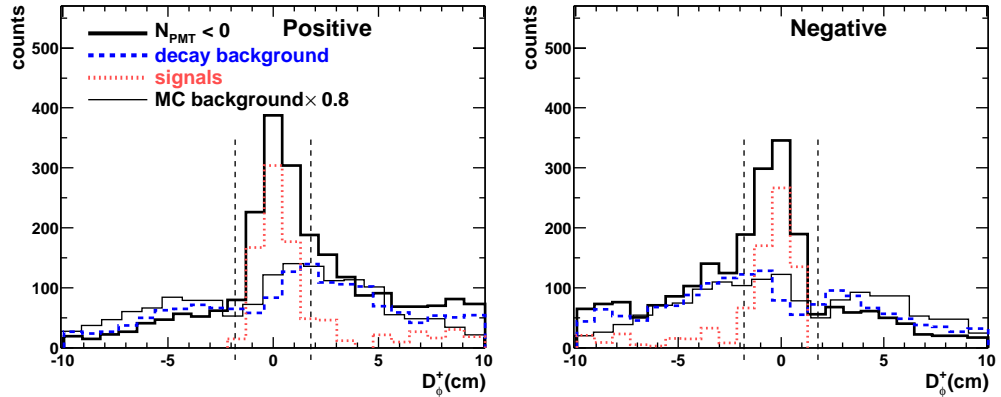


FIG. 4: An illustration of the track match in D_ϕ^+ for tracks without an associated RICH PMT and with $6 < p_T < 7$ GeV/c, shown for minimum bias events and separately for positive (left) and negative (right) charged tracks. The first three distributions represent the raw counts for all tracks without a RICH association (thick solid line), estimated decay backgrounds (dashed line), and signal tracks (dot-dashed line) that were calculated as the difference of the two. The thin solid line represents the matching distribution of decay background from Monte-carlo simulation, arbitrarily scaled to match the data. The 2σ matching window are illustrated by the vertical dashed line. Outside the signal window, the shape of the dashed line matches the solid line rather well, the difference of 10% level is taken into account in the error estimation of R_{decay} .

4 GeV/c the signal-to-background ratio is about 10, and decreases to 1 at 7.5 GeV/c and to ~ 0.3 at 10 GeV/c.

Weak decays of short lived particles, mainly K_s^0 , Λ and $\bar{\Lambda}$ within the magnetic field provide an additional source of background. A significant fraction of this background is subtracted using the R_{decay} method described above. However, secondary particles from decays close to the event vertex are not subtracted since they are nearly indistinguishable from primary particles. This “feed-down” contaminates the track sample without the associated RICH PMTs, S_{NR} (about 40% of all charged particles at high p_T), and needs to be subtracted from

the data.

To estimate the feed-down contribution we generate $Au + Au$ events with HIJING [38], reconstruct them through the PHENIX Monte-Carlo simulation, and count the secondaries which survive all analysis cuts. The secondaries from Λ and $\bar{\Lambda}$ decays are counted relative to the reconstructed $(p + \bar{p})$, and correspondingly, those from K_s^0 relative to $(K^+ + K^-)/2$. We tune the $(\Lambda + \bar{\Lambda})/(p + \bar{p})$, $K_s^0/(0.5(K^+ + K^-))$ ratios by weighting the particle distributions generated according to HIJING such that they reproduce the nearly p_T -independent experimentally observed ratios from $Au + Au$ collisions at $\sqrt{s_{NN}} = 130$

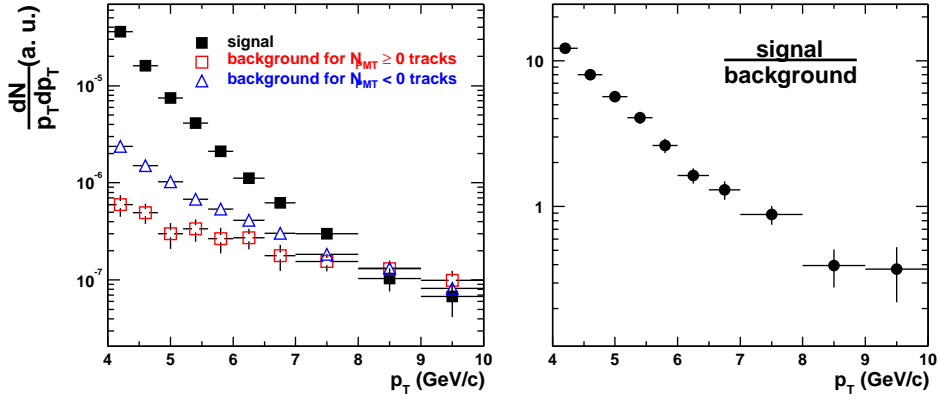


FIG. 5: Amount of background estimated as function of p_T for minimum bias collisions. The left figure shows the background subtracted charged hadron spectra (filled square), the background from γ conversions (open square) and decays (open triangle). The right figure shows the signal to background ratio. Only statistical errors are shown.

GeV [39, 40].

The final feed-down contribution depends on the choice of the Λ and K_s^0 p_T spectra and of their yields in the high p_T range where they are not measured. Both yields and spectral shapes are varied within limits imposed by the spectrum for tracks that doesn't fire the RICH. The average feed-down contribution depends on p_T and varies between 6 to 13% relative to the total charged hadron yield; it is subtracted from the charged spectra. The systematic uncertainties are estimated from the spread of the feed-down contributions obtained with different assumptions. The uncertainties are approximately 60% of the subtraction, and depend on p_T and centrality.

Table II summarizes the systematic errors on the background subtraction ². All errors are correlated with p_T and are presented as relative errors to the charged hadron yield. The uncertainty of the pion-loss ($\delta_{\pi loss}$) was rescaled by the fraction of signal tracks with RICH association, i.e. $S_R/(S_R + S_{NR})$. Errors on the scaling factors R_e and R_{decay} were individually folded with the signal-to-background ratios in the two samples. The resulting uncertainties on the charged yields were then added in quadrature ($\delta_{R_e \oplus R_{decay}}$). The uncertainty of the K_s^0 , Λ , and $\bar{\Lambda}$ feed-down subtraction is denoted by $\delta_{feeddown}$.

E. Corrections and systematic uncertainties

After background subtraction, we have determined a single, p_T -dependent correction function to correct the hadron spectra for acceptance, decay in flight, reconstruction efficiency and momentum resolution. This function is determined using a GEANT [41] Monte-Carlo

simulation of the PHENIX detector in which simulated single tracks are reconstructed using the same analysis chain applied to the real data. Because of decays and multiple scattering, the correction function depends on the particle species. This is reflected in Fig. 6, where the correction functions averaged between π^+ and π^- , K^+ and K^- , p^+ and p^- are shown separately. At $p_T < 3$ GeV/c, the kaon correction function is significantly larger than those for pions and protons; For $p_T > 3$ GeV/c, this difference is less than 15%. To take into account this species dependence, we determine the correction function separately for pions, kaons, protons, and their anti-particles. The final correction function is then obtained by combining the correction functions for the different particle species weighted by the measured p_T -dependent particle composition from [42]. Above 2 GeV/c, where kaon data are not available, we assume the K/π ratio is constant within $\pm 10\%$ from the value observed at 2 GeV/c. This assumption leads to a 2.5% systematic error in the correction function. The resulting correction function is plotted in the upper left panel of Fig. 7. The sharp rise below 2 GeV/c is due to loss in acceptance and decays in flight. Above 2 GeV/c, the correction decreases only slowly with p_T . For $p_T > 4$ GeV/c, the correction varies by less than $\pm 5\%$.

The data are also corrected for efficiency losses due to detector occupancy. Though this is negligible for peripheral collisions, these losses are important in central collisions, and are evaluated by embedding simulated tracks into real events. The average track reconstruction efficiency in the active detector area is larger than 98% for peripheral collisions, but decreases to $70 \pm 3.5\%$ for central collisions. As shown in the lower part of Fig. 7, the efficiency loss is independent of p_T within a $\pm 3\%$ systematic uncertainty from 1.5 to 10 GeV/c. Based on this observation, the full correction can be factorized into centrality-dependent (i.e. detector occupancy dependent) correction function, $c(N_{part})$, and p_T -dependent correction function, $c(p_T)$. The centrality-dependent cor-

² We should emphasize that, in the remaining discussion unless stated otherwise, all systematic errors listed in Tables have been adjusted to 1σ errors.

TABLE II: Systematic errors on background subtraction. All errors are given in percent and are quoted as 1σ errors. These errors are correlated with p_T .

p_T (GeV/c)	$\delta_{\pi loss}$ (%)	$\delta_{R_e \oplus R_{decay}}$ (%)	$\delta_{feeddown}$ (%)	total(%)
< 5	0.3	0.3	5	5
5 - 6	0.6	1.8	5	5.3
6 - 7	1.4	4.1	8.5	9.5
7 - 8	4.6	7.1	7.8	11.5
8 - 9	9.9	17.6	6	21.1
9 - 10	19.4	23.5	6	31.1

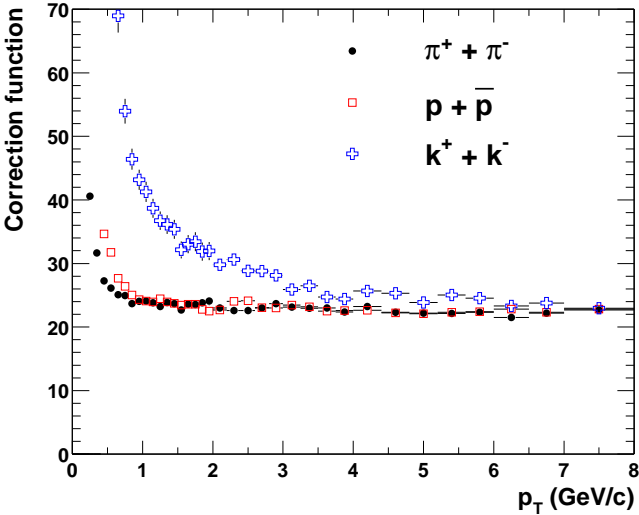


FIG. 6: Averaged correction functions for π^+ and π^- , p and \bar{p} , and K^+ and K^- .

rection function is shown on the upper right panel of Fig. 7. Most of the efficiency loss is due to hit overlaps, which can shift the hit positions in the DC or PC's outside of the matching windows. The $\pm 2\sigma$ matching windows are larger at low p_T to account for multiple scattering (see Eq. 3), thus the tracks are less vulnerable to the effect of hit merging. This effect has been taken into account by applying a slightly smaller, p_T -dependent, occupancy correction at $p_T < 1.5$ GeV/c.

Figure 7 also shows systematic errors on the correction functions. These errors include not only the errors on the correction itself, but also the uncertainty due to the background subtraction procedure.

Finally, the inclusive charged hadron yield are obtained by multiplying the p_T -dependent correction function, $c(p_T)$, and centrality-dependent correction function, $c(N_{part})$, with the background subtracted spectra and dividing by the number of events for every centrality class as:

$$\frac{1}{N_{evts}} \frac{dN}{2\pi p_T dp_T d\eta} = \frac{1}{N_{evts}} \times c(p_T) \times c(N_{part}) \quad (8)$$

$$\times \left(\frac{dN}{p_T dp_T d\eta} \right)^{bgr-subtracted}$$

The systematic errors on the spectra, which are common to all centrality classes, are listed in Table III. Sources of systematic uncertainties are: the matching cuts (δ_{match}), normalization (δ_{norm}), particle composition (δ_{mix}), momentum resolution (δ_{reso}), momentum scale (δ_{scale}), and background subtraction (δ_{bgr}) from Table II. The normalization error is independent of p_T . All other errors vary with p_T but are highly correlated bin-to-bin, which means that points in neighboring p_T bins can move in the same direction by similar factors.

The centrality-dependent systematic errors are quantified in terms of the central-to-peripheral ratio, R_{cp} , as given in Table IV. Besides the uncertainty on the occupancy correction ($\delta_{occupancy}$) illustrated in Fig. 7, the background subtraction procedure has a centrality-dependent uncertainty. As discussed in Section II D, the errors on R_e and R_{decay} reflect the p_T and centrality dependencies. The centrality-dependent part contributes about half of the error on both R_e and R_{decay} , and hence does not cancel in R_{cp} . Since the errors on R_e and R_{decay} are independent, the uncertainty on R_{cp} is approximately equal to $\delta_{R_e \oplus R_{decay}}$ from Table II. Finally, $\delta_{feeddown}$ is the centrality-dependent error from feed-down subtraction.

III. RESULTS

A. Inclusive charged hadron p_T spectra

Figure 8 shows the inclusive charged hadron p_T spectra for various centrality classes. All spectra exhibit power-law tails at high p_T . But for peripheral collisions, the power-law shape is more concave than for central collisions. More details of the centrality dependence of the spectral shape can be seen from Fig. 9, which shows for each centrality class the ratio of the spectra to the minimum-bias spectrum. In these ratios, most systematic errors cancel or affect the overall scale only. The characteristic centrality dependence of the shape already observed in $\sqrt{s_{NN}} = 130$ GeV $Au + Au$ collisions [18, 19] is more apparent at $\sqrt{s_{NN}} = 200$ GeV. In peripheral collisions, the ratio decreases up to $p_T \sim 2$ GeV/c and then rises up to about 4 GeV/c. The trends are reversed in the most central collisions. In the range above 4–5 GeV/c, all ratios appear to be constant as function of p_T , which

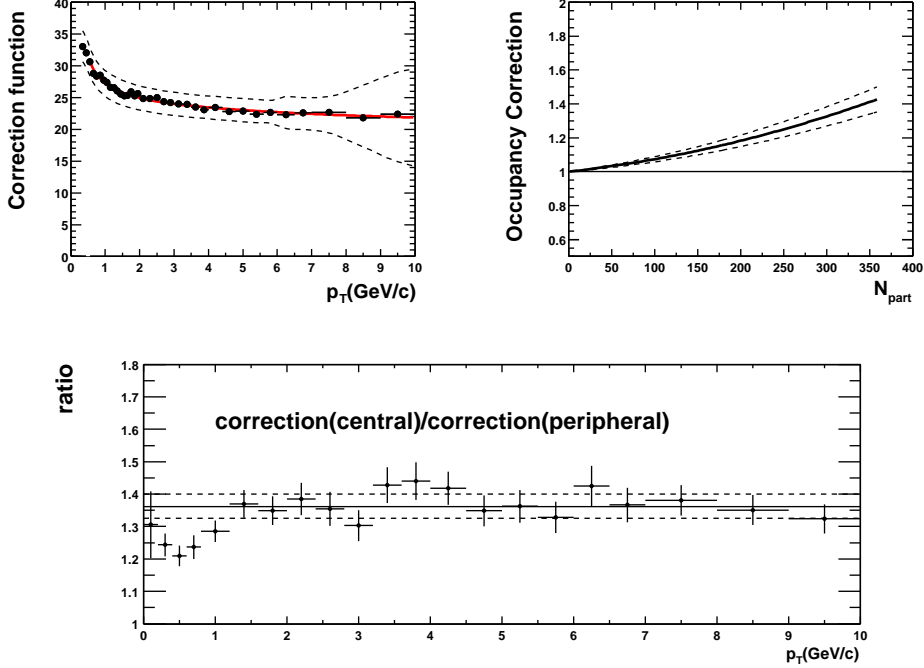


FIG. 7: Functions used to correct the charged particle p_T spectra. The upper left panel shows the p_T dependent correction, $c(p_T)$. The upper right panel shows the centrality dependent correction, $c(N_{part})$. Systematic uncertainties are indicated by the dashed lines. The two corrections factorize at $p_T > 1.5$ GeV/c, so that for given centrality the full correction function is given by $c(p_T) \times c(N_{part})$. The accuracy of this factorization is demonstrated in the lower panel. The ratio of the full correction for central collisions (5% most central) to the correction for single particle events varies by less than 3% above 1.5 GeV/c (the error bar is the statistical error from the Monte-Carlo calculation).

TABLE III: Systematic errors on the p_T spectra. All errors are given in percent and are quoted as 1σ errors. They are either normalization errors or are p_T correlated errors.

p_T (GeV/c)	$\delta_{match}(\%)$	$\delta_{norm}(\%)$	$\delta_{mix}(\%)$	$\delta_{reso}(\%)$	$\delta_{scale}(\%)$	$\delta_{bgr}(\%)$	total(%)
< 1	3.5	3.2	2.4	0.6	0.6	5	7.3
1 - 5	3	3.2	2.4	0.6	3	5	7.6
5 - 6	3	3.2	1.8	0.6	3.6	5.3	7.9
6 - 7	3	3.2	1.8	0.6	3.3	9.5	11.1
7 - 8	3	3.2	1.8	0.6	3.1	11.5	12.8
8 - 9	3	3.2	1.8	0.9	3.1	21.1	21.9
9 - 10	3	3.2	1.8	5.3	3.1	31.1	32.1

would imply that they have a similar centrality independent shape.

Based on the different trends observed in Fig. 9, we can distinguish three p_T regions: 0.5–2, 2–4.5 and > 4.5 GeV/c. The different centrality dependence of the spectral shape in these regions can be quantified by a truncated average p_T :

$$\langle p_T^{trunc} \rangle \equiv \frac{\int_{p_T^{min}}^{8 \text{ GeV}/c} p_T \cdot dN/dp_T}{\int_{p_T^{min}}^{8 \text{ GeV}/c} dN/dp_T} - p_T^{min}, \quad (9)$$

which is insensitive to the normalization of the spectra. The upper bound of 8 GeV/c in the integral is given by

the limited p_T reach for peripheral centrality classes as shown in Fig. 8. In Fig 10, the values of $\langle p_T^{trunc} \rangle$ for the three p_T^{min} values are plotted as function of centrality, represented by the average number of participating nucleons (N_{part}) for each centrality class.

For $p_T^{min} = 0.5$ GeV/c, where particle production is expected to be governed by soft physics, $\langle p_T^{trunc} \rangle$ increases with N_{part} . This trend is also seen for the average p_T of identified charged hadrons, and reflects the increased radial flow of soft particles in more central collisions [42]. For $p_T^{min} = 2$ GeV/c, the trend is significantly different. For peripheral collisions, $\langle p_T^{trunc} \rangle$ is substantially larger than the value obtained with $p_T^{min} = 0.5$ GeV/c due to the presence of the power-law tail. With increasing N_{part} ,

TABLE IV: Systematic errors on the central-to-peripheral ratio. All errors are given in percent and are quoted as 1σ errors. Most of the systematic errors listed in Table III cancel in the central-to-peripheral ratio. Only those errors that are uncorrelated with centrality are shown here.

p_T (GeV/c)	$\delta_{occupancy}$ (%)	$\delta_{feeddown}$ (%)	$\delta_{R_c \oplus R_{decay}}$ (%)	total (%)
< 6	5	5	1.8	7.3
6 - 7	5	5	4.1	8.2
7 - 8	5	5	7.1	10
8 - 9	5	5	17.6	19
9 - 10	5	5	23.5	24.6

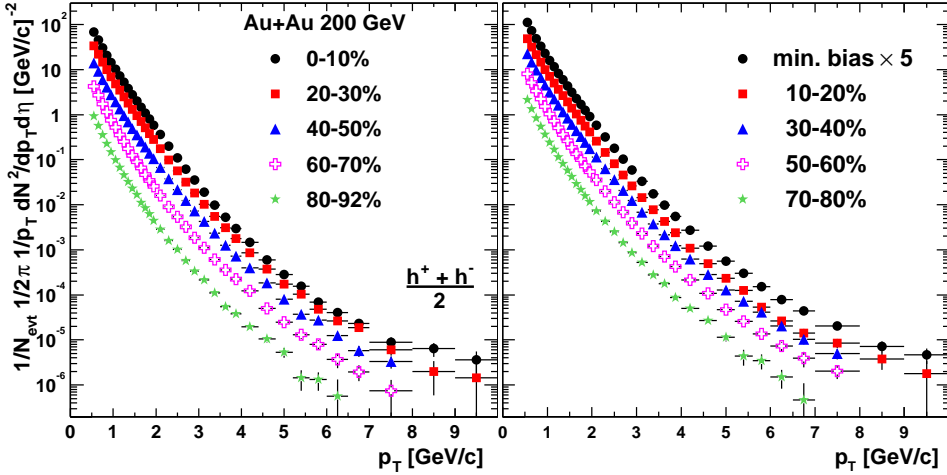


FIG. 8: p_T spectra of charged hadrons for minimum bias collisions along with spectra for 9 centrality classes. The minimum bias spectrum has been multiplied by 5 for visibility. Only statistical errors are shown in the spectra. Most of the p_T dependent systematic errors are independent of centrality and are tabulated in Table III.

$\langle p_T^{trunc} \rangle$ for $p_T^{min} = 2 GeV/c decreases and the values obtained with $p_T^{min} = 0.5$ and 2 GeV/c approach each other, which indicates an almost exponential spectrum in central collisions around ~ 2 GeV/c. For the highest p_T range ($p_T^{min} = 4.5$ GeV/c), $\langle p_T^{trunc} \rangle$ is approximately constant. This implies that the shape of the spectrum is nearly independent of centrality, as would be expected if this region is dominated by hard scattering.$

However, the yields at high p_T do not scale with the number of nucleon-nucleon collisions; they are suppressed comparing to the binary collision scaling expected for hard scattering processes. This can be clearly seen from Fig. 11, which shows R_{cp} , the ratio of yields for central and peripheral collisions normalized to the average number of nucleon-nucleon collisions in each event sample. The ratio is below unity for all p_T . The three p_T regions show different trends as outlined in the discussion of Fig. 10: (i) In the “soft” region with $p_T < 2$ GeV/c, the ratio increases as function of p_T . (ii) In the “hard” region with $p_T > 4.5$ GeV/c, the suppression appears to be constant at ~ 0.3 , which again indicates that the spectra have a similar shape, but with the yield in central collisions being suppressed by a constant factor from 4.5 to 10 GeV/c. (iii) In the transition region from 2 to ~ 4.5 GeV/c, the ratio decreases as function of p_T .

B. Suppression of high p_T hadrons in $Au + Au$ at $\sqrt{s_{NN}} = 200$ GeV

At finite Q^2 , nuclear modifications of the parton distribution [43] and initial [25, 44] and final state [10] interactions of the scattering partons can modify the high- p_T hadron production rates in hard scattering processes. Medium modifications of hadron spectra are often quantified by the “nuclear modification factor” R_{AA} , which we calculate for each centrality class as the ratio of the yield per nucleon-nucleon collision in $Au + Au$ to the yield in nucleon-nucleon collisions:

$$R_{AA}(p_T, \eta) = \left(\frac{1}{N_{evt}} \frac{d^2 N^{A+A}}{dp_T d\eta} \right) / \left(\frac{\langle N_{coll} \rangle}{\sigma_{inel}^{N+N}} \frac{d^2 \sigma^{N+N}}{dp_T d\eta} \right) \quad (10)$$

$\langle N_{coll} \rangle / \sigma_{inel}^{N+N}$ is the average Glauber nuclear overlap function, $\langle T_{AuAu} \rangle$, for each centrality class. In order to calculate R_{AA} , we need a reference spectrum for nucleon-nucleon collisions. Due to the lack of charged hadron data with sufficient reach in p_T from our own experiment, we construct the $N + N$ reference for charged hadrons from the π^0 spectra in $p + p$ collisions at $\sqrt{s} = 200$ GeV/c measured by PHENIX [16], and the charged hadron to pion ratio observed in other experiments, as described below.

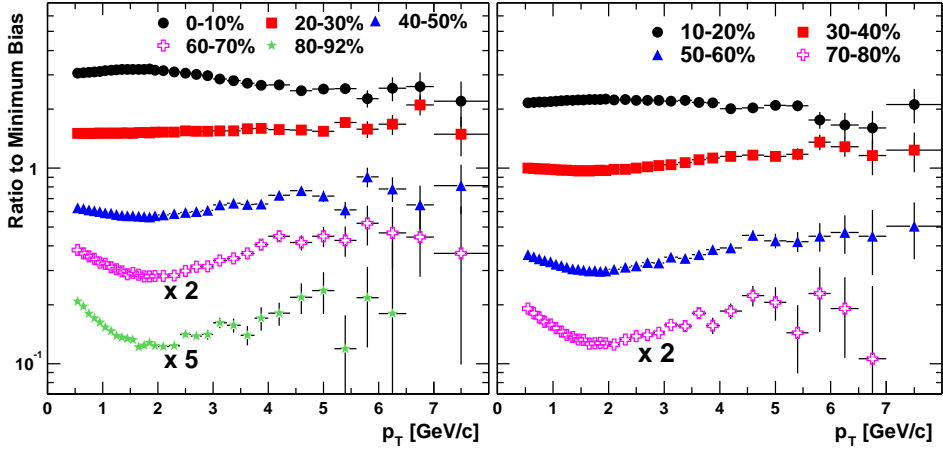


FIG. 9: Ratios of centrality selected p_T spectra to the minimum bias spectrum. Ratios for peripheral classes are scaled up for clarity. For the p_T range shown, most of the systematic errors cancel in the ratio. The remaining systematic errors that can change the shape are less than 10% (see Table IV) and are correlated bin-to-bin in p_T .

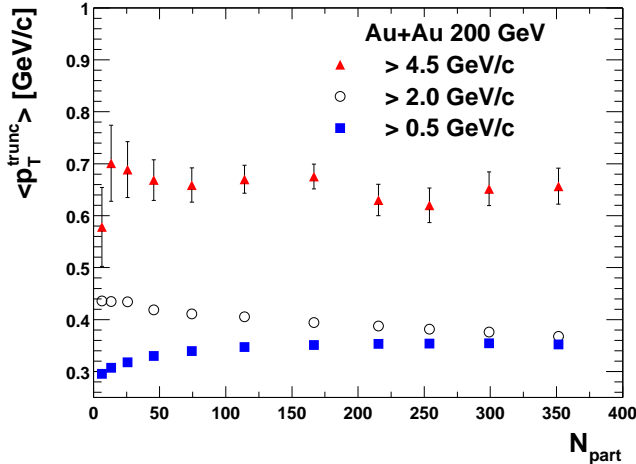


FIG. 10: Centrality dependence of $\langle p_T^{trunc} \rangle$, defined as the average p_T of charged particles with p_T above a threshold p_T^{min} minus the threshold p_T^{min} (see Eq. 9). Shown are $\langle p_T^{trunc} \rangle$ values for three p_T^{min} cuts, with $p_T^{min} = 0.5, 2$ and $4.5 \text{ GeV}/c$ respectively. Only statistical errors are shown.

The PHENIX π^0 spectra from $p + p$ collisions are measured out to $14 \text{ GeV}/c$. These data can be parameterized by a power-law function,

$$\frac{d^2\sigma_{N+N}^{\pi^0}}{\sigma_{inel}^{N+N} dp_T d\eta} = \frac{A}{\sigma_{inel}} \left(\frac{p_0}{p_0 + p_T} \right)^n , \quad (11)$$

with $A = 386 \text{ mb/GeV}^2$, $p_0 = 1.219 \text{ GeV}$, and $n = 9.99$ [16].

In $p + p$ experiments at the ISR, the h/π ratio was measured to be 1.6 ± 0.16 , independent of p_T from 1.5 to $5 \text{ GeV}/c$, and independent of \sqrt{s} from 23 to 63 GeV [30]. Below $1.5 \text{ GeV}/c$, h/π decreases towards lower p_T . The ISR data are consistent with data on π, K, P production from FNAL E735 experiment [45] at $\sqrt{s} = 1.8 \text{ TeV}$. The

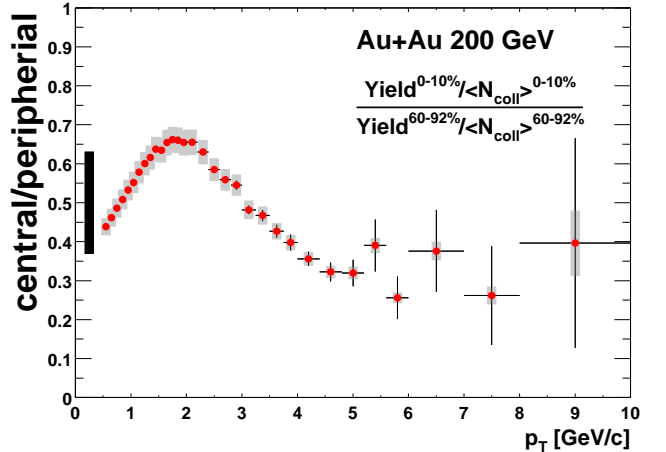


FIG. 11: Ratio of charged hadron yields per nucleon-nucleon collision between central (0-10%) and peripheral (60-92%) $Au + Au$ collisions. In this ratio, most of the systematic errors cancel. The solid error bars on each data point are statistical. The error bar on the left hand side of the figure is the overall scale error relative to 0.5, which is the quadrature sum of (i) the uncertainty of $\langle N_{coll} \rangle$ (see Table I) and (ii) the uncertainty on the occupancy correction ($\delta_{occupancy}$). The shaded error band on each data point is the p_T dependent systematic error from $\delta_{Re \oplus R_{decay}}$ and centrality dependent feed down correction ($\delta_{feeddown}$) as given in Table IV.

h/π ratio computed from these data increases with p_T and reaches a value of 1.6 at the end of the measured p_T range, $\sim 1.5 \text{ GeV}/c$. At high momentum, a h/π ratio of ~ 1.6 is also observed for quark and gluon jet fragmentation in e^+e^- collisions at LEP by the DELPHI Collaboration [31]. Finally, charged hadron data measured by PHENIX in $p + p$ collisions and UA1 [46] in $\bar{p} + p$ collisions, both at $\sqrt{s} = 200 \text{ GeV}/c$, give consistent h/π ratios when compared to the PHENIX $p + p \pi^0$ data.

Based on these findings, we assume that h/π is constant above 1.5 GeV/c in $p + p$ collisions at RHIC and that we can scale up the π^0 cross-section (Eq. 11) by this factor to obtain a reference for charged hadron production. To be consistent with the data described above, we correct this reference below 1.5 GeV/c using,

$$r(p_T) = \begin{cases} R_{h/\pi} - a(p_{max} - p_T)^2 & \text{for } p_T \leq p_{max} \\ R_{h/\pi} & \text{for } p_T > p_{max} \end{cases}, \quad (12)$$

where $R_{h/\pi} = 1.6$, $p_{max} = 1.6$ GeV/c and $a = 0.28$ GeV $^{-2}$. The charged hadron reference used in this analysis is then given by the product of the power-law function from Eq. 11 and the empirical correction from Eq. 12 as:

$$\frac{d^2\sigma_{N+N}^{h^+ + h^-}}{\sigma_{inel}^{N+N} dp_T d\eta} = \frac{A}{\sigma_{inel}} \left(\frac{p_0}{p_0 + p_T} \right)^n \times r(p_T) \quad . \quad (13)$$

The systematic errors on the charged hadron $N + N$ reference are summarized in Table V. The main sources of uncertainties include: (i) the systematic errors on the absolute normalization of the PHENIX π^0 data ($\delta_{norm}^{\pi^0}$), which are independent of p_T , (ii) uncertainties due to the power-law fit to the π^0 data ($\delta_{fit}^{\pi^0}$), and (iii) uncertainties on $R_{h/\pi}$ ($\delta_{h/\pi}$), which are estimated from the spread of $R_{h/\pi}$ obtained from different data sets used to constrain h/π^0 .

Figure 12 shows the nuclear modification factor $R_{AA}(p_T)$ for charged hadrons from minimum bias and nine centrality classes. The systematic errors on R_{AA} are described in the figure captions. At low p_T , the charged hadron R_{AA} increase monotonically up to 2 GeV/c for all centrality classes. At $p_T > 2$ GeV/c, R_{AA} remains constant and close to unity for the most peripheral centrality class. However, in central collisions, it decreases at higher p_T , down to an approximately constant value of 0.2–0.3 for $p_T > 4$ –5 GeV/c. This is consistent with Fig. 11, where the central to peripheral ratio also saturates above 4–5 GeV/c. This approximately p_T independent suppression pattern has been interpreted as a result of the detailed interplay between the Cronin effect, nuclear shadowing, and partonic energy loss [47].

Also shown in Fig. 12 are R_{AA} for neutral pions from ref. [21]. The neutral pion R_{AA} values also seem to reach maximum around 2 GeV/c, but the changes are smaller than those for charged hadrons. Except for the most peripheral bin, the neutral pion R_{AA} are always below the charged R_{AA} in the range of $2 < p_T < 4.5$ GeV/c. However, at $p_T > 4.5$ GeV/c, R_{AA} for both neutral pions and hadrons saturate at roughly the same level, indicating a similar suppression for neutral pions and charged hadrons at high p_T .

The fact that the neutral pion R_{AA} values are smaller than inclusive charged hadron R_{AA} at intermediate p_T ($2 < p_T < 4.5$ GeV/c) has already been observed at $\sqrt{s_{NN}} = 130$ GeV [17]. This difference can be explained by the large p/π ratio observed in the same p_T range in

central $Au + Au$ collisions [27, 28]. This large relative proton and anti-proton yield indicates a deviation from the standard picture of hadron production at $p_T > 2$ GeV/c, which assumes that the hadrons are created by the fragmentation of energetic partons. Such a deviation has led to models of quark coalescence [32] or baryon junctions [48] as the possible mechanisms to enhance the proton production rate at medium p_T . Both models predict that baryon enhancement is limited to $p_T < 5$ GeV/c, beyond which jet fragmentation should eventually become the dominant production mechanism for all particle species. In that case, one would expect a similar suppression factor for charged hadron and π^0 , in agreement with the data at $p_T > 4.5$ GeV/c. Recently, the difference of R_{AA} between charged hadrons and pions was also argued as the consequence of centrality and particle species dependent $\langle k_T \rangle$ broadening effect [49].

If hard-scattering dominates charged hadron production at $p_T > 4.5$ GeV/c, the particle composition should be determined by the jet fragmentation function, similar to nucleon-nucleon collisions. Fig. 13 shows h/π^0 for all centrality classes. The systematic errors are explained in the figure captions. In the most peripheral collisions, the h/π^0 ratio is consistent with the $p + p$ values down to $p_T \approx 2$ GeV/c. In central collisions, the h/π^0 ratio is enhanced by as much as 50% above the $p + p$ value in the region $1 < p_T < 4.5$ GeV/c. This enhancement gradually decreases towards more peripheral collisions and reflects the difference of R_{AA} between the charged hadrons and π^0 s, which is due to large baryon contribution. The enhancement also strongly depends on p_T : It reaches a maximum between 2.5 and 3.5 GeV/c, then decreases. At $p_T > 4.5$ GeV/c, the h/π^0 ratios for all centralities reach an approximately constant value of 1.6, which is consistent with the h/π value observed in $p + p$ [30] collisions and in jet fragmentation in e^+e^- [31] collisions. The similarity of the spectral shape and of the particle composition between $Au + Au$ and $p + p$ collisions suggest that fragmentation of hard-scattered partons indeed is the dominant mechanism of particle production in $Au + Au$ collisions above p_T of 4–5 GeV/c, regardless of the fact that the yields do not scale with N_{coll} .

Since R_{AA} values for charged hadrons and π^0 s are approximately constant at $p_T > 4.5$ GeV/c, we can quantify the centrality dependence of the R_{AA} value by calculating it from yields integrated above 4.5 GeV/c. The upper panel of Figure 14 shows R_{AA} for $p_T > 4.5$ GeV/c as function of N_{part} . The R_{AA} values for charged hadrons and π^0 agree for all centrality classes within errors. In peripheral collisions with $N_{part} < 50$, R_{AA} is consistent with binary collision scaling. With increasing N_{part} , R_{AA} decreases monotonically, reaching a value of 0.23 ± 0.03 (0–5% most central) for charged hadrons and 0.24 ± 0.02 (0–10% most central) for π^0 s. There is an additional 14% error common to charged hadrons and π^0 s, which originates from the uncertainty on the NN reference and N_{coll} .

To address suggestions that the yield of high p_T

TABLE V: Systematic errors on the charged hadron $N + N$ reference spectrum. All errors are given in percent and are quoted as 1σ errors. Most of the errors are correlated with p_T .

p_T (GeV/c)	$\delta_{norm}^{\pi^0}$ (%)	$\delta_{fit}^{\pi^0}$ (%)	$\delta_{R_{h/\pi}}$ (%)	total (%)
0.75	10.4	-3.9 + 9.1	-15.1 + 5.9	-18.7 + 15.0
1.00	10.4	-4.1 + 8.9	-14.4 + 5.9	-18.3 + 14.9
1.50	10.4	-4.6 + 8.3	-11.6 + 5.9	-16.3 + 14.6
2.00	10.4	-5.1 + 7.7	-7.9 + 5.9	-14.0 + 14.2
2.50	10.4	-5.5 + 7.2	-5.9 + 5.9	-13.1 + 13.9
3.00	10.4	-5.9 + 6.7	-5.9 + 5.9	-13.3 + 13.7
3.50	10.4	-6.4 + 6.4	-5.9 + 5.9	-13.5 + 13.5
4.50	10.4	-7.5 + 6.5	-5.9 + 5.9	-14.1 + 13.6
5.50	10.4	-8.9 + 7.9	-5.9 + 5.9	-14.9 + 14.3
6.50	10.4	-10.7 + 10.5	-5.9 + 5.9	-16.0 + 15.9
7.50	10.4	-12.9 + 14.3	-5.9 + 5.9	-17.6 + 18.7
8.50	10.4	-15.8 + 19.4	-5.9 + 5.9	-19.8 + 22.8
9.50	10.4	-19.3 + 25.9	-5.9 + 5.9	-22.7 + 28.5

hadrons in $Au + Au$ collisions may be proportional to N_{part} instead of N_{coll} [25, 50], we have investigated a different ratio,

$$R_{AA}^{N_{part}} = 2\langle N_{coll} \rangle / \langle N_{part} \rangle \times R_{AA} \quad . \quad (14)$$

$R_{AA}^{N_{part}}$ for $p_T > 4.5$ GeV/c is shown in the lower panel of Fig. 14, together with solid (or dashed) bands representing the allowed range if the data follow binary collision (or participant) scaling. As discussed above, for peripheral collisions, $R_{AA}^{N_{part}}$ follows more closely the binary collision scaling. Above 50 participants, $R_{AA}^{N_{part}}$ varies by only $\pm 20\%$. However, it peaks at $\langle N_{part} \rangle = 100$ and decreases monotonically towards more central collisions³.

The decrease of $R_{AA}^{N_{part}}$ could be a natural consequence of energy loss of hard scattered partons in the medium [50]. If the energy loss is large, hard scattered partons may only escape near the surface of the reaction volume. In a cylindrical collision geometry, for which the number of collisions from the surface is proportional to N_{part} , binary collision scaling is reduced to an approximate participant scaling. Detailed calculations show that in this case, $R_{AA}^{N_{part}}$ slightly decreases with N_{part} depending in details on how the energy loss is modelled [50]. This interpretation is also consistent with our previous conclusion that, above 4.5 GeV/c, hadron production is dominated by hard-scattering although the yield does not scale with the number of binary collisions. Gluon saturation

scenarios [25] also suggest approximate participant scaling. However, the same models suggest a 30% increase in $R_{AA}^{N_{part}}$ over the p_T range 4.5–9 GeV/c in central collisions that is not observed in the data (compare with upper right panel in Fig. 12).

C. Energy dependence and x_T scaling

The inclusive charged hadron and π^0 p_T spectra and h/π^0 ratios suggest that fragmentation of hard scattered partons is the dominant production mechanism of high p_T hadrons not only in $p + p$ but also in $Au + Au$ collisions. For $p + p$ collisions this fact was demonstrated on general principles well before the advent of QCD by the method of “ x_T -scaling”. This method does not depend on whether the initial projectiles are protons or Au ions, so it should be directly applicable to $Au + Au$ collisions. Since our data show a suppression of high- p_T particles in central $Au + Au$ collisions with respect to point-like scaling from $p + p$ and peripheral $Au + Au$ collisions, it is important to investigate whether the production dynamics of high- p_T particles in central (and peripheral) $Au + Au$ collisions are the same or different from those in $p + p$ collisions. We first review the x_T -scaling method in $p + p$ collisions and then apply it to the present $Au + Au$ data.

The idea of hard-scattering in $N + N$ collisions dates from the first indication of point-like structure inside the proton, in 1968, found in deep inelastic electron-proton scattering [51], i.e. scattering with large values of 4-momentum transfer squared, Q^2 , and energy loss, ν . The discovery that the Deep Inelastic Scattering (DIS) structure function

$$F_2(Q^2, \nu) = F_2 \left(\frac{Q^2}{\nu} \right) \quad (15)$$

³ In the p_T range from 3–4 GeV/c, $R_{AA}^{N_{part}}$ for charged hadrons is approximately constant, which is consistent with earlier measurements at $\sqrt{s_{NN}} = 130$ GeV [19] and $\sqrt{s_{NN}} = 200$ GeV [20]. To interpret this constancy as participant scaling is misleading, since pion and proton yields change differently with centrality in this p_T region, and $R_{AA}^{N_{part}}$ accidentally appears constant for inclusive charged hadron. The data above 4.5 GeV/c shown in Fig. 14 are free of this effect.

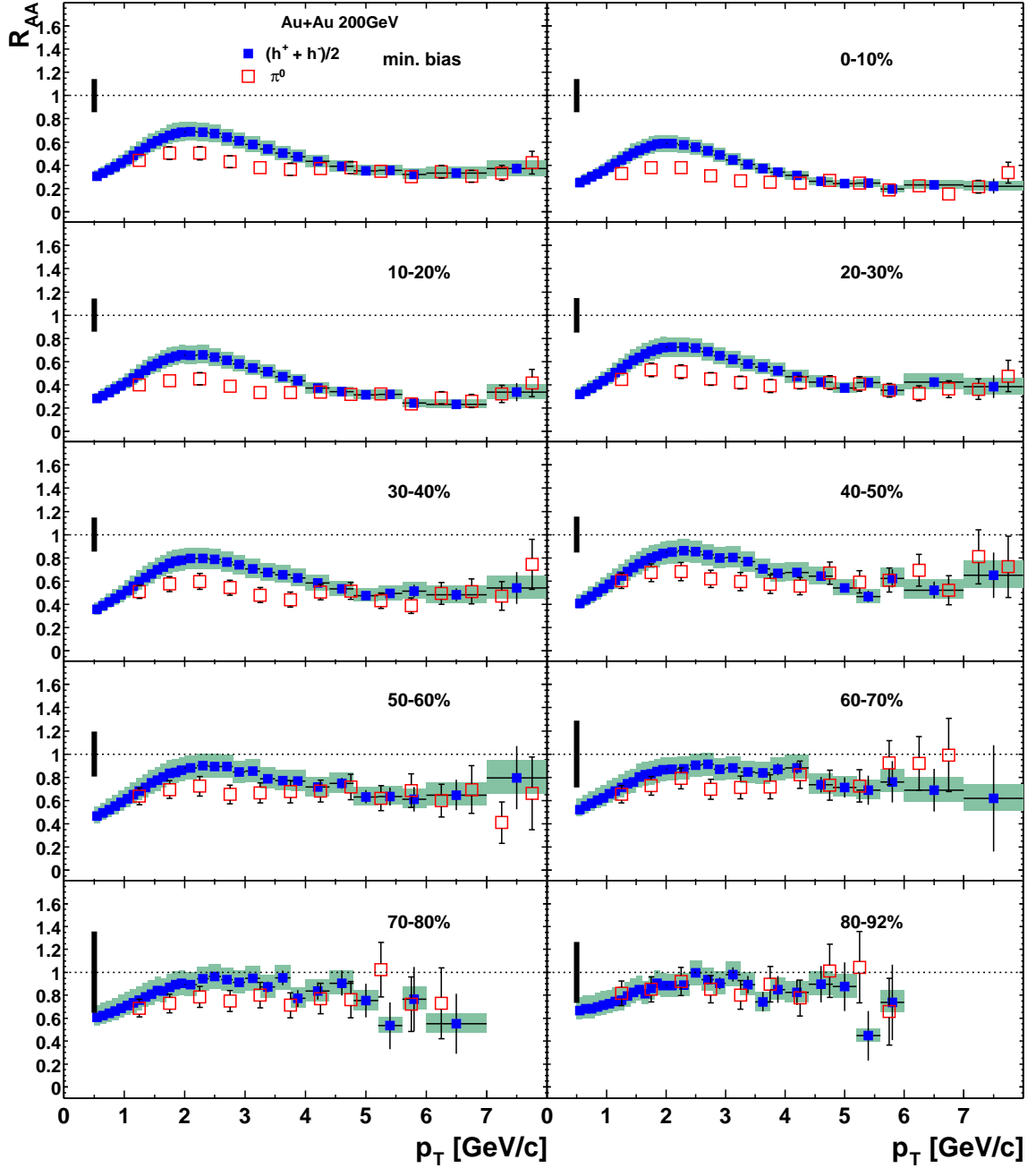


FIG. 12: R_{AA} for $(h^+ + h^-)/2$ and π^0 as function of p_T for minimum bias and 9 centrality classes according to the “Fine” type of centrality classes defined in Table I. The error bars on the π^0 data points include statistical and systematical errors on the $Au + Au$ data and the $N + N$ reference. The error bars on $(h^+ + h^-)/2$ data points are statistical errors only. The normalization errors on the reference common for charged hadrons and π^0 s are added in quadrature with the uncertainty on $\langle N_{coll} \rangle$ and are indicated by the black bar on the left side of each panel. This error ranges from 15% to 36% from central to peripheral collisions and can shift all points in the charged and neutral pion R_{AA} up and down together. The shaded band on charged R_{AA} includes the remaining systematic errors on the charged $N + N$ reference summed in quadrature with the systematic errors from the $Au + Au$ spectra. This error amounts to $-12.5\% - +18\%$ at low p_T and changes to $\pm 12.5\%$ at $p_T = 4.5$ GeV/c and $\pm 18.5\%$ at $p_T = 8$ GeV/c .

“scales”, or in other words, depends on the ratio

$$x = \frac{Q^2}{2M\nu} \quad (16)$$

independent of Q^2 as suggested by Bjorken [52], led to the concept of a proton being composed of point-like “partons”. Since the partons of DIS are charged, and hence must scatter electromagnetically from each other in $p + p$ collisions, a general formula for the cross section of the single-particle inclusive reaction

$$p + p \rightarrow C + X \quad (17)$$

was derived [53] using the principle of factorization of the reaction into parton distribution functions for the protons, fragmentation functions to particle C for the scattered partons and a short-distance parton-parton hard scattering cross section.

The invariant cross section for the single-particle inclusive reaction (Eq. 17), where particle C has transverse momentum p_T near mid-rapidity, was given by the general scaling form [54]:

$$E \frac{d^3\sigma}{dp^3} = \frac{1}{p_T^n} F \left(\frac{2p_T}{\sqrt{s}} \right) \quad \text{where} \quad x_T = 2p_T/\sqrt{s} \quad . \quad (18)$$

The cross section has 2 factors: a function F which depends only on the ratio of momenta, and a dimensioned factor, p_T^{-n} , where n depends on the quantum exchanged in the hard-scattering. For QED or Vector Gluon exchange [53], $n = 4$. For the case of quark-meson scattering by the exchange of a quark [54], $n=8$. The discovery of high p_T pions in $p + p$ scattering at the CERN-ISR, in 1972 [55, 56, 57], at a rate much larger than predicted by electromagnetic scattering, but with the scaling form of Eq. 18, proved that the partons of DIS strongly interact with each other.

Inclusion of QCD [58] into the scaling form led to the x_T -scaling law (Eq. 18),

$$E \frac{d^3\sigma}{dp^3} = \frac{1}{\sqrt{s}^{n(x_T, \sqrt{s})}} G(x_T) \quad , \quad (19)$$

where the “ x_T -scaling power” $n(x_T, \sqrt{s})$ should equal 4 in lowest order (LO) calculations, analogous to the $1/q^4$ form of Rutherford Scattering in QED. The structure and fragmentation functions, which scale as the ratios of momenta are all in the $G(x_T)$ term. Due to higher order effects such as the running of the coupling constant, $\alpha_s(Q^2)$, the evolution of the structure and fragmentation functions, and the initial state k_T , measured values of $n(x_T, \sqrt{s})$ in $p + p$ collisions are in the range from 5 to 8.

The compilation of single particle inclusive transverse momentum spectra at mid-rapidity from $p + p$ and $p + \bar{p}$ collisions at c.m. energy \sqrt{s} from 23 to 1800 GeV [30, 46, 59] is shown in Fig. 15a for $(h^+ + h^-)/2$, and in Fig. 16a for π^0 [16, 60, 61, 62, 63]. The spectra exhibit a characteristic shape: an exponential part

at low $p_T \leq 1$ GeV/ c which depends very little on \sqrt{s} (soft physics), and a power-law tail for $p_T \geq 2$ GeV/ c which depends very strongly on \sqrt{s} (hard physics). The high p_T part of the spectra shows a characteristic scaling behavior indicative of fragmentation of jets produced by hard-scattering of the quark and gluon constituents of the proton as described by QCD [64, 65, 66]. The x_T -scaling of the single particle inclusive data is nicely illustrated by a plot of

$$\sqrt{s}^{n(x_T, \sqrt{s})} \times E \frac{d^3\sigma}{dp^3} = G(x_T) \quad , \quad (20)$$

as a function of x_T , with $n(x_T, \sqrt{s}) = 6.3$. The $(h^+ + h^-)/2$ data (Fig. 15b) show an asymptotic power law with increasing x_T . Data at a given \sqrt{s} fall below the asymptote at successively lower values of x_T with increasing \sqrt{s} , corresponding to the transition region from hard to soft physics in the p_T range of 1–2 GeV/ c . The π^0 data (Fig. 16b) show a similar x_T -scaling but without the deviation at low x_T , since all available data are for p_T larger than 1–2 GeV/ c . For larger $x_T \geq 0.3$, a value of $n = 5.1$ [60, 67] improves the scaling for the 3 lower c.m. energies, $\sqrt{s} = 38.7, 52.7$ and 62.4 GeV. It will be a challenge at RHIC to obtain data in this x_T range to see whether the value of $n \sim 5$ is the asymptotic limit for inclusive single particle production or whether n reaches the (LO) QCD value of 4. x_T -scaling has also been studied in jet production at $\sqrt{s} = 630$ and 1800 GeV [68], where $n = 4.45$ is observed in the jet x_T range 0.15–0.3.

In $Au + Au$ collisions, x_T -scaling should work just as well as in $p + p$ collisions and should yield the same value of $n(x_T, \sqrt{s})$ if the high p_T particles are the result of hard-scattering according to QCD. This is because the structure and fragmentation functions in $Au + Au$ collisions should scale, so that Eq. 19 applies, albeit with a different $G(x_T)$. Thus, if the suppression of high- p_T particles with respect to point-like scaling from $p + p$ collisions is due to shadowing of the structure functions [43] or gluon saturation [25], which are basically scaling effects⁴, rather than due to a final state interaction with the dense medium, the cross sections (Eq. 19) at a given x_T (and centrality) should all exhibit the same suppression. The initial state shadowing may cause $G(x_T)$ to change with centrality, but $n(x_T, \sqrt{s})$ should remain constant. In the case of the interaction with the dense medium, x_T -scaling may or may not hold, depending on the details of the energy loss, for instance, whether or not the energy loss of the hard-scattered parton scales with its energy. It is also conceivable that the high p_T particles observed in $Au + Au$ collisions at RHIC have nothing to do with QCD hard-scattering [26, 32, 48]. In this case, striking

⁴ There is a slight non scaling effect of the structure functions [43] since for fixed x_T , Q^2 changes by a factor of 2.4 between the two $\sqrt{s_{NN}}$.

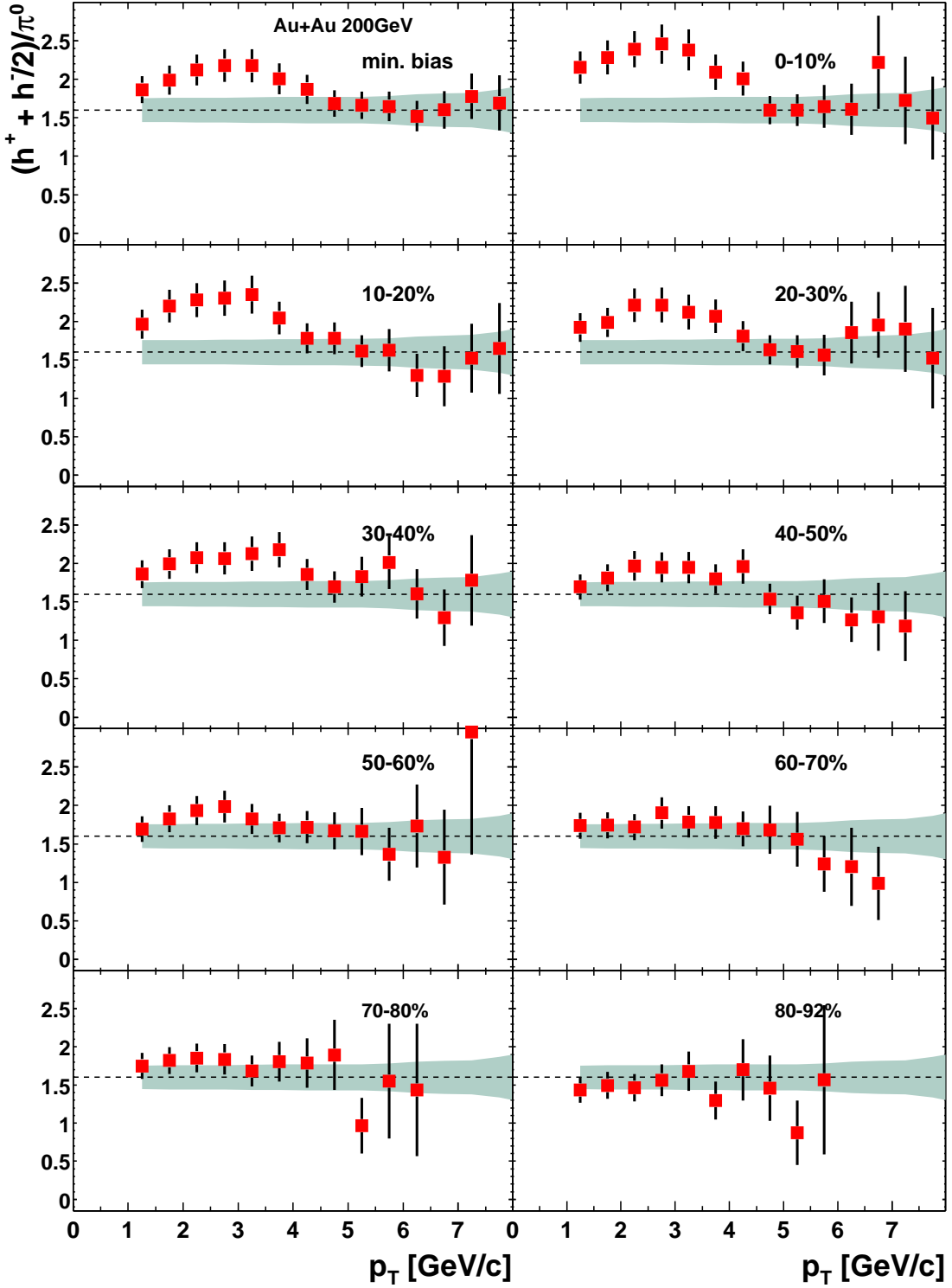


FIG. 13: Charged hadron to π^0 ratios for minimum bias events and 9 centrality classes according to the “*Fine*” type of centrality classes defined in Table I. The error bars represent the quadratic sum of statistical and point-by-point systematic errors from $(h^+ + h^-)/2$ and π^0 . The shaded band shows the percent normalization error (dominantly from $(h^+ + h^-)/2$ data) common to all centrality classes. The dashed line at 1.6 is the h/π ratio measured in $p + p$ [30] and e^+e^- [31] collisions.

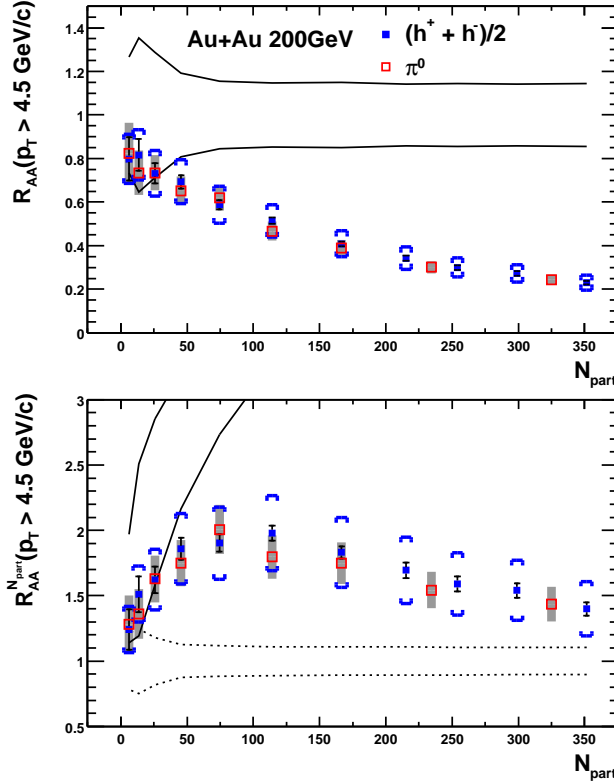


FIG. 14: $Au + Au$ yield integrated for $p_T > 4.5$ GeV/c over the $N + N$ yield, normalized using either N_{coll} (R_{AA} in the top panel) or N_{part} ($R_{AA}^{N_{part}}$ in the bottom panel), plotted as function of $\langle N_{part} \rangle$. “Fine” and “Coarse” types of the centrality classes defined in Table I are used for $(h^+ + h^-)/2$ and π^0 , respectively. Following errors are shown in both figures: i). The bands denoted by solid (dashed) lines represent the binary collision (participant pair) scaling. The width of the bands represent the systematic errors due to the normalization errors common to $(h^+ + h^-)/2$ and π^0 added in quadrature with the uncertainty on $\langle N_{coll} \rangle$ ($\langle N_{part} \rangle$). These errors can move $(h^+ + h^-)/2$ and π^0 up and down together in centrality correlated way, and are the same as the black error bars discussed in Fig. 12. ii). The error bars for each $(h^+ + h^-)/2$ data point are statistical error. The p_T correlated systematic errors from $Au + Au$ and the rest of the systematic errors on the charged hadron $N + N$ reference are represented by the brackets, within which the charged hadron data points can move up or down relative to π^0 . iii). Dark shaded error bands around each π^0 data point include both statistical and point-to-point systematic errors on $Au + Au$ and the π^0 $N + N$ reference.

differences from Eq. 19 and the systematics observed in $p + p$ collisions should be expected.

To test x_T -scaling in $Au + Au$ collisions, we plot the quantities defined by Eq. 20 in Fig. 17 for charged hadron and π^0 data from $\sqrt{s_{NN}} = 130$ GeV and 200 GeV for central (0-10%) and peripheral (60-80%) collisions. For the power n , we use the same value $n(x_T, \sqrt{s}) = 6.3$ that was used for the $p + p$ data shown in Fig. 15b and Fig. 16b. The data are consistent with x_T -scaling over

the range $0.03 \leq x_T \leq 0.06$ for π^0 and $0.04 \leq x_T \leq 0.075$ for $(h^+ + h^-)/2$.

According to Eq. 19, the ratio of inclusive cross sections at fixed x_T equals $(200/130)^n$. Thus, the power $n(x_T, \sqrt{s})$ is related directly to the logarithm of the ratio of invariant hadron yield at fixed x_T as:

$$n(x_T) = \frac{\log(yield(x_T, 130\text{GeV})/yield(x_T, 200\text{GeV}))}{\log(200/130)}. \quad (21)$$

The power n ’s for both neutral pions and charged hadrons for central and peripheral collisions are shown in Fig. 18. While the π^0 data in central and peripheral collisions and charged hadron data in peripheral collisions seem to favor a similar power n , the charged hadron data from central collisions require a larger value of n .

For a more quantitative analysis, the $Au + Au$ data for a given centrality and hadron selection are fitted simultaneously for $\sqrt{s_{NN}} = 130$ and 200 GeV to the form,

$$\left(\frac{A}{\sqrt{s}}\right)^n (x_T)^{-m}, \quad (22)$$

where we have approximated Eq. 19 by using a constant power $n(x_T, \sqrt{s})$ and a power-law, x_T^{-m} , for $G(x_T)$ over a limited range in x_T . The fit results and errors are quoted in Table VI. The corresponding ratios of yields are presented by lines in Fig. 18, where the fit ranges ($0.03 \leq x_T \leq 0.06$ for π^0 ’s and $0.04 \leq x_T \leq 0.074$ for charged hadrons) are indicated by the length of the line.

For peripheral collisions the fitted values for the power are $n = 6.33 \pm 0.54$ and $n = 6.12 \pm 0.49$, for π^0 and charged hadrons respectively, which are in quantitative agreement with the expectation from $p + p$ collisions. Approximate x_T -scaling in peripheral $Au + Au$ collisions with the same power as observed in $p + p$ collisions indicates that hard-scattering is the dominating production mechanism for high p_T particles. In central collisions, neutral pions also exhibit x_T -scaling with a similar power, $n = 6.41 \pm 0.55$. Thus, it seems that high- p_T π^0 production is consistent with hard-scattering for all centralities.

For charged hadrons, the power found for central collisions is $n = 7.53 \pm 0.44$. Most of the systematic errors are common and cancel between central and peripheral collisions, thus the difference of the two powers found for charged hadrons, $\Delta n = n_{cent} - n_{periph} = 1.41 \pm 0.43$ compared with that for neutral pion $\Delta n = 0.09 \pm 0.47$, is significant.

This difference is consistent with the large proton and anti-proton enhancement in central $Au + Au$ collisions for intermediate p_T seen at $\sqrt{s_{NN}} = 130$ and 200 GeV, which appears to violate x_T -scaling. The x_T range $0.04 \leq x_T \leq 0.074$ corresponds to $4 < p_T < 7.4$ GeV/c at $\sqrt{s_{NN}} = 200$ GeV, but it corresponds to $2.6 < p_T < 4.8$ GeV/c at $\sqrt{s_{NN}} = 130$ GeV. If protons are enhanced at $2 < p_T < 4.5$ GeV/c in central collisions at both $\sqrt{s_{NN}} = 130$ GeV and 200 GeV, then n_{cent} will be larger than n_{periph} in the measured x_T range. Since $\sqrt{s_{NN}} = 200$

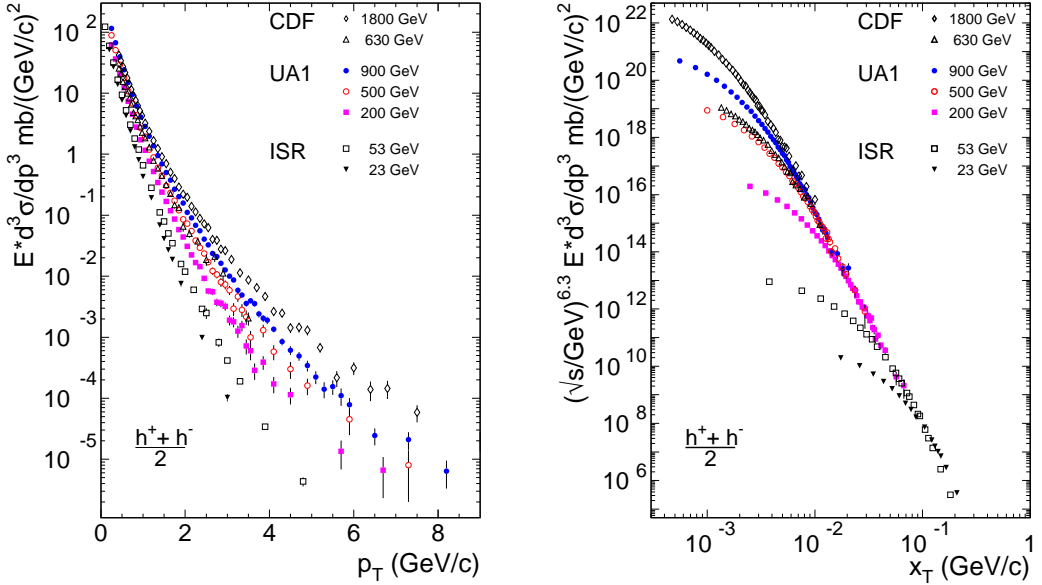


FIG. 15: (a) CDF, UA1 and ISR transverse momentum dependence of the invariant cross section at seven center of mass energies from different experiments [30, 46, 59]. (b) The same data multiplied by $\sqrt{s}^{6.3}$, plotted as a function of $x_T = 2p_T/\sqrt{s}$.

TABLE VI: Results of the simultaneous fit to $\sqrt{s_{NN}} = 130$ and 200 GeV data using Eq. 22. The fit ranges are $0.03 \leq x_T \leq 0.06$ for π^0 and $0.04 \leq x_T \leq 0.074$ for charged hadron. Only statistical and point-to-point systematic errors on the data points are included in the fit, which gives the statistical error on n . The normalization errors and other p_T correlated systematic errors are not included in the fit but are directly translated into a systematic error on n .

Fitting results for π^0 over $0.03 < x_T < 0.06$		
parameters	0-10% centrality bin	60-80% centrality bin
A	0.973 ± 0.232	0.843 ± 0.3
m	8.48 ± 0.17	7.78 ± 0.22
n	$6.41 \pm 0.25(\text{stat})$ $\pm 0.49(\text{sys})$	$6.33 \pm 0.39(\text{stat})$ $\pm 0.37(\text{sys})$
Fitting results for $h^+ + h^-$ over $0.04 < x_T < 0.074$		
A	2.30 ± 0.44	0.62 ± 0.27
m	8.74 ± 0.28	8.40 ± 0.43
n	$7.53 \pm 0.18(\text{stat})$ $\pm 0.40(\text{sys})$	$6.12 \pm 0.33(\text{stat})$ $\pm 0.36(\text{sys})$

GeV data indicate that the proton enhancement is limited to the medium p_T range, based on the equality of R_{AA} for charged hadrons and π^0 at $p_T > 4.5$ GeV/c (Fig. 12), this difference should go away at larger x_T .

IV. SUMMARY

We have presented a systematic study of the p_T and centrality dependence of charged hadron production at $|\eta| < 0.18$ at $\sqrt{s_{NN}} = 200$ GeV. The yields per nucleon-nucleon collision in central collisions are significantly suppressed compared to peripheral and nucleon-nucleon collisions. The suppression is approximately independent of p_T above 4.5 GeV/c for all centrality classes, suggesting a similar spectral shape between $Au + Au$ and $p + p$ collisions. At $p_T > 4.5$, charged hadron suppression is the same as for neutral pions; the ratio h/π^0 is ~ 1.6 for all centralities, similar to the h/π value measured in $p + p$ and e^+e^- collisions. The similar spectral shape and particle composition at high p_T are consistent with jet fragmentation as the dominating mechanism of particle production in $Au + Au$ collisions for $p_T > 4-5$ GeV/c. For both charged hadrons and neutral pions, the suppression sets in gradually from peripheral to central collisions, consistent with the expectation of partonic energy loss and surface emission of high p_T hadrons. x_T -scaled hadron yields are compared between $\sqrt{s_{NN}} = 130$ GeV and $\sqrt{s_{NN}} = 200$ GeV $Au + Au$ collisions. We find that the x_T scaling power n calculated for neutral pions in central and peripheral collisions and charged hadron in peripheral collisions is 6.3 ± 0.6 , similar to $p + p$ collisions. This again points towards similar production dynamics, i.e. hard-scattering processes as described by QCD. However, n is 7.5 ± 0.5 for charged hadrons in

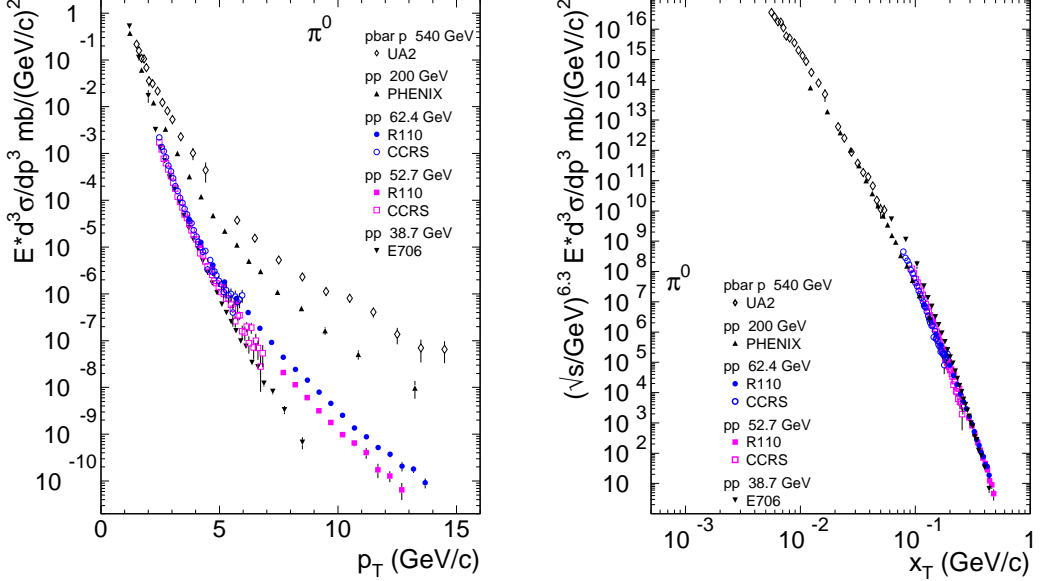


FIG. 16: (a) Transverse momentum dependence of the invariant cross section for π^0 at five center-of-mass energies from different experiments [16, 60, 61, 62, 63]. (b) The same data multiplied by $\sqrt{s}^{6.3}$, plotted vs $x_T = 2p_T/\sqrt{s}$.

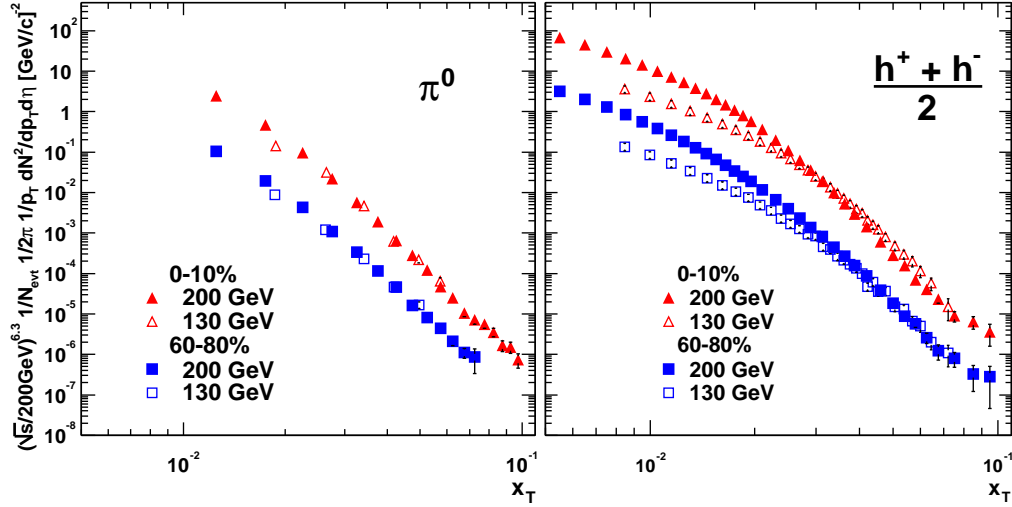


FIG. 17: x_T scaled spectra for central collisions and peripheral collisions at $\sqrt{s_{NN}} = 130$ and 200 GeV. The left figure shows the π^0 x_T spectra, and the right figure shows the $(h^+ + h^-)/2$ x_T spectra. The central (0-10%) x_T spectra are represented by triangular symbols, and the peripheral (60-80%) x_T spectra are represented by square symbols. The open symbols represent x_T spectra from $\sqrt{s_{NN}} = 130$ GeV scaled by a factor of $(130/200)^{6.3}$. The solid symbols represent x_T spectra from $\sqrt{s_{NN}} = 200$ GeV. The error bars are statistical only.

central collisions, indicating a strong non-scaling modification of particle composition of charged hadron spectra from that of $p + p$ at intermediate p_T , 2–4.5 GeV/c. This is consistent with the large h/π^0 ratios observed over the same p_T range in central collisions.

Acknowledgments

We thank the staff of the Collider-Accelerator and Physics Departments at Brookhaven National Laboratory and the staff of the other PHENIX participating institutions for their vital contributions. We acknowl-

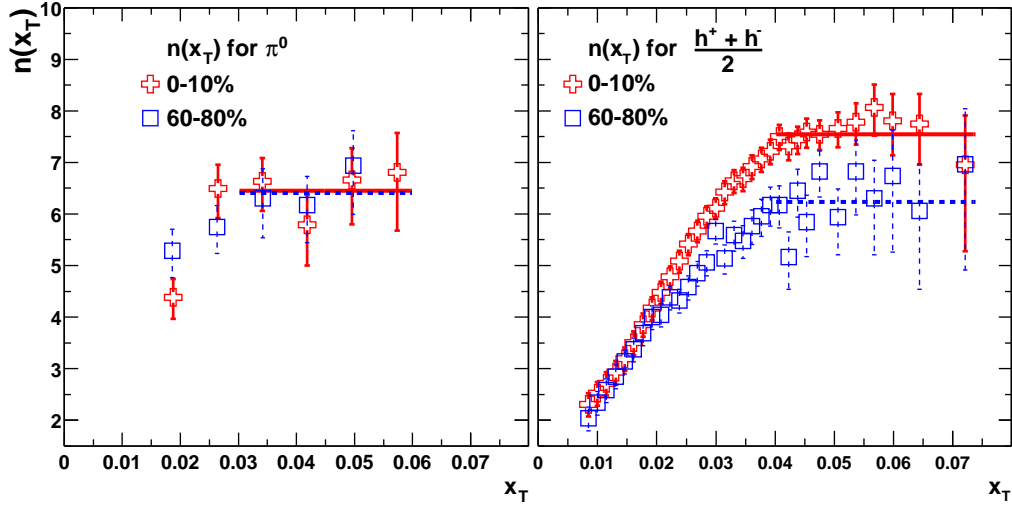


FIG. 18: The x_T scaling power n (according to Eq. 21) plotted as function of x_T calculated for π^0 (top-left) and $(h^+ + h^-)/2$ (top-right) in central (0-10%) and peripheral (60-80%) collisions. The solid (and dashed) lines indicate a constant fit along with the fitting ranges to the central (and peripheral) $n(x_T)$ functions. The error bars at each data point include statistical and point-to-point systematic errors from $\sqrt{s_{NN}} = 130$ and 200 GeV. The scale errors on x_T spectra are 20.7% (15.9%) for π^0 x_T spectra ratio in central (peripheral) collisions, and 18.6% (15.7%) for $(h^+ + h^-)/2$ x_T spectra ratio in central (peripheral) collisions. These type of errors propagate into the systematic errors on x_T scaling power n listed in Table VI.

edge support from the Department of Energy, Office of Science, Nuclear Physics Division, the National Science Foundation, Abilene Christian University Research Council, Research Foundation of SUNY, and Dean of the College of Arts and Sciences, Vanderbilt University (U.S.A), Ministry of Education, Culture, Sports, Science, and Technology and the Japan Society for the Promotion of Science (Japan), Conselho Nacional de Desenvolvimento Científico e Tecnológico and Fundação de Amparo à Pesquisa do Estado de São Paulo (Brazil), Natural Science Foundation of China (People's Republic of China), Centre National de la Recherche Scientifique, Commissariat à l'Énergie Atomique, Institut National de Physique Nucléaire et de Physique des Particules, and Institut National de Physique Nucléaire et de Physique des Particules, (France), Bundesministerium fuer Bil-

dung und Forschung, Deutscher Akademischer Austausch Dienst, and Alexander von Humboldt Stiftung (Germany), Hungarian National Science Fund, OTKA (Hungary), Department of Atomic Energy and Department of Science and Technology (India), Israel Science Foundation (Israel), Korea Research Foundation and Center for High Energy Physics (Korea), Russian Ministry of Industry, Science and Technologies, Russian Academy of Science, Russian Ministry of Atomic Energy (Russia), VR and the Wallenberg Foundation (Sweden), the U.S. Civilian Research and Development Foundation for the Independent States of the Former Soviet Union, the US-Hungarian NSF-OTKA-MTA, the US-Israel Binational Science Foundation, and the 5th European Union TMR Marie-Curie Programme.

[1] F. Karsch, Lect. Notes. Phys. **583**, 209 (2002).
[2] See Proceedings Quark Matter 1984, edited by K. Kajantie (Springer, Berlin, 1985); Proceedings Quark Matter 1987, edited by H. Satz, H.J. Specht, and R. Stock, Z. Phys. **C38**, 1 (1988).
[3] NA49 Collaboration, T. Alber *et. al.*, Phys. Rev. Lett. **75**, 3814 (1995).
[4] PHENIX Collaboration, K. Adcox *et al.*, Phys. Rev. Lett. **87**, 052301 (2001).
[5] PHENIX Collaboration, A. Bazilevsky *et al.*, Nucl. Phys. **A715**, 486 (2003).
[6] J.D. Bjorken, Phys. Rev. **D27**, 140 (1983).
[7] D. Teaney *et al.*, Phys. Rev. Lett. **86**, 4783 (2001).
[8] P. Huovinen *et al.*, Phys. Lett. **B503**, 58 (2001); U. Heinz and P. Kolb, Nucl. Phys. **A702**, 269 (2002).
[9] W. Broniowski and W. Florkowski, Phys. Rev. Lett. **87**, 272302 (2001); W. Florkowski and W. Broniowski, Phys. Rev. **C65**, 064905 (2002).
[10] M. Gyulassy and M. Plümer, Phys. Lett. **B243**, 432 (1990); X.N. Wang and M. Gyulassy, Phys. Rev. Lett. **68**, 1480 (1992); R. Baier *et al.*, Phys. Lett. **B345**, 277 (1995).
[11] R. Baier, D. Schiff, and B.G. Zakharov, Ann. Rev. Nucl. Part. Sci. **50**, 37 (2000).
[12] R. Baier, Y.L. Dokshitzer, A.H. Mueller, and D. Schiff, J. High Energy Phys. **9**, 33 (2001).
[13] X.N. Wang, Phys. Rev. **C63**, 054902 (2001).
[14] X.N. Wang, Nucl. Phys. **A715**, 775 (2003).

- [15] J.F. Owens *et al.*, Phys. Rev. **D18**, 1501 (1978).
- [16] PHENIX Collaboration, S.S. Adler *et al.*, hep-ex/0304038, submitted to Phys. Rev. Lett.
- [17] PHENIX Collaboration, K. Adcox *et al.*, Phys. Rev. Lett. **88**, 022301 (2002).
- [18] STAR Collaboration, C. Adler *et al.*, Phys. Rev. Lett. **89**, 202301 (2002).
- [19] PHENIX Collaboration, K. Adcox *et al.*, Phys. Lett. **B561**, 82 (2003).
- [20] PHOBOS Collaboration, B.B. Back *et al.*, nucl-ex/0302015, submitted to Phys. Lett. **B**.
- [21] PHENIX Collaboration, S.S. Adler *et al.*, nucl-ex/0304022.
- [22] STAR Collaboration, J. Adams *et al.*, nucl-ex/0305015.
- [23] M. Gyulassy, I. Vitev and X.N. Wang, Phys. Rev. Lett. **86**, 2537 (2001).
- [24] G.G. Barnafoldi, P. Levai, G. Papp, G. Fai, and Y. Zhang, nucl-th/0212111.
- [25] D. Kharzeev, E. Levin and L. McLerran, Phys. Lett. **B561**, 93 (2003), and references therein.
- [26] K. Gallmeister, C. Greiner, and Z. Xu, nucl-th/0202051; K. Gallmeister, C. Greiner, and Z. Xu, Phys. Rev. **C67**, 244905 (2003).
- [27] PHENIX Collaboration, K. Adcox *et al.*, Phys. Rev. Lett. **88**, 242301 (2002).
- [28] PHENIX Collaboration, S.S. Adler *et al.*, nucl-ex/0305036.
- [29] STAR Collaboration, J. Adams *et al.*, nucl-ex/0306007.
- [30] B. Alper *et al.*, Nucl. Phys. **B100**, 237 (1975).
- [31] P. Abreu *et al.*, Eur. Phys. J. **C17**, 207 (2000); O. Klapp, Doctoral Thesis, *Eine umfassende Studie der Eigenschaften von Quark and Gluon Jets*, University Wuppertal 1999.
- [32] R.C. Hwa and C.B. Yang, Phys. Rev. **C67**, 034902 (2003); R.J. Fries, B. Müller, C. Nonaka, and S.A. Bass, nucl-th/0301087, to appear in Phys. Rev. Lett. ; V. Greco, C.M. Ko, and P. Levai, Phys. Rev. Lett. **90**, 202302 (2003); V. Greco, C.M. Ko, and P. Levai, nucl-th/0305024; R.J. Fries, B. Müller, C. Nonaka, and S.A. Bass, nucl-th/0306027.
- [33] K. Adcox *et al.*, Nucl. Instrum. Methods **A499**, 469 (2003).
- [34] R.J. Glauber and G. Matthiae, Nucl. Phys. **B21**, 135 (1970).
- [35] Woods-Saxon Au nuclear radius $R = 6.38^{+0.27}_{-0.13}$ fm, diffusivity $a = 0.53 \pm 0.01$ fm [B. Hahn, D.G. Ravenhall, and R. Hofstadter, Phys. Rev. **101**, 1131 (1956)], and nucleon-nucleon cross section $\sigma_{NN}^{inel} = 42 \pm 3$ mb.
- [36] K. Adcox *et al.*, Nucl. Instrum. Methods **A499**, 489 (2003); J.T. Mitchell *et al.*, Nucl. Instrum. Methods **A482**, 491 (2002).
- [37] M. Aizawa *et al.*, Nucl. Instrum. Methods **A499**, 508 (2003).
- [38] X.N. Wang and M. Gyulassy, Phys. Rev. **D44**, 3501 (1991).
- [39] PHENIX Collaboration, K. Adcox *et al.*, Phys. Rev. Lett. **89**, 092302 (2002).
- [40] STAR Collaboration, C. Adler *et al.*, nucl-ex/0206008.
- [41] GEANT 3.2.1, CERN program library.
- [42] PHENIX Collaboration, S.S. Adler *et al.*, nucl-ex/0307022.
- [43] K.J. Eskola, V.J. Kolhinen, and P.V. Ruuskanen, Nucl. Phys. **B535**, 351 (1998); K.J. Eskola, V.J. Kolhinen, and C.A. Salgado, Eur. Phys. J. **C9**, 61 (1999).
- [44] D. Antreasyan *et al.*, Phys. Rev. **D19**, 764 (1979).
- [45] T. Alexopoulos *et al.*, Phys. Rev. **D48**, 984 (1993).
- [46] C. Albajar *et al.*, Nucl. Phys. **B335**, 261 (1990).
- [47] I. Vitev and M. Gyulassy, Phys. Rev. Lett. **89**, 252301 (2002).
- [48] I. Vitev and M. Gyulassy, Phys. Rev. **C65**, 041902(R) (2002).
- [49] Xiaofei Zhang and George Fai, hep-ph/0306227.
- [50] B. Müller, Phys. Rev. **C67**, 061901 (2003).
- [51] M. Breidenbach *et al.*, Phys. Rev. Lett. **23**, 935 (1969); see also W.K.H. Panofsky, in *Proceedings of the Fourteenth International Conference On High Energy Physics*, Vienna, Austria, 1968 (CERN Scientific Information Service, Geneva, Switzerland, 1968), p. 23.
- [52] J.D. Bjorken, Phys. Rev. **D179**, 1547 (1969).
- [53] S.M. Berman, J.D. Bjorken, and J.B. Kogut, Phys. Rev. **D4**, 3388 (1971).
- [54] R. Blankenbecler, S.J. Brodsky, and J.F. Gunion, Phys. Lett. **B42**, 461 (1972).
- [55] F.W. Büsser *et al.*, Phys. Lett. **B46**, 471 (1973), see also *Proc. 16th Int. Conf. HEP*, edited by J.D. Jackson and A. Roberts, (NAL, Batavia, IL, 1972) Vol. 3, p. 317.
- [56] M. Banner *et al.*, Phys. Lett. **B44**, 537 (1973).
- [57] B. Alper *et al.*, Phys. Lett. **B44**, 521 (1973).
- [58] R.F. Cahalan, K.A. Geer, J. Kogut, and L. Susskind,
- [59] F. Abe *et al.*, Phys. Rev. Lett. **61**, 1819 (1988).
- [60] A.L.S. Angelis *et al.*, Phys. Lett. **B79**, 505 (1978). See also, A.G. Clark *et al.*, Phys. Lett. **B74**, 267 (1978).
- [61] F.W. Büsser *et al.*, Nucl. Phys. **B106**, 1 (1976).
- [62] M. Banner *et al.*, Phys. Lett. **B115**, 59 (1982); M. Banner *et al.*, Z. Phys. **C27**, 329 (1985).
- [63] L. Apanasevich *et al.*, hep-ex/0204031.
- [64] L. DiLella, Ann. Rev. Nucl. Part. Sci. **35**, 107 (1985).
- [65] P. Darriulat, Ann. Rev. Nucl. Part. Sci. **30**, 159 (1980).
- [66] J.F. Owens, Rev. Mod. Phys. **59**, 465 (1987). Phys. Rev. **D11**, 1199 (1975).
- [67] C. Kourkoumelis *et al.*, Phys. Lett. **B84**, 271 (1979).
- [68] J. Huston, *Proc. 29th Int. Conf. HRP (ICHEP 98)*, Vancouver, Canada, 1998 (World Scientific Singapore, 1999), hep-ph/9901352.